

Spring 2011

## Hydrostatic Pressure Testing of a Square-Cross Section Stainless Steel Propellant Tank Manufactured Using Selective Laser Sintering

Spencer Fuller

*Embry-Riddle Aeronautical University - Daytona Beach*

Follow this and additional works at: <https://commons.erau.edu/db-theses>



Part of the [Aerospace Engineering Commons](#)

---

### Scholarly Commons Citation

Fuller, Spencer, "Hydrostatic Pressure Testing of a Square-Cross Section Stainless Steel Propellant Tank Manufactured Using Selective Laser Sintering" (2011). *Theses - Daytona Beach*. 68.

<https://commons.erau.edu/db-theses/68>

This thesis is brought to you for free and open access by Embry-Riddle Aeronautical University – Daytona Beach at ERAU Scholarly Commons. It has been accepted for inclusion in the Theses - Daytona Beach collection by an authorized administrator of ERAU Scholarly Commons. For more information, please contact [commons@erau.edu](mailto:commons@erau.edu).

**HYDROSTATIC PRESSURE TESTING OF A  
SQUARE-CROSS SECTION  
STAINLESS STEEL PROPELLANT TANK  
MANUFACTURED USING SELECTIVE LASER SINTERING**

**By  
Spencer Fuller**

**A Thesis Submitted to the  
Graduate Studies Office  
In Partial Fulfillment of the Requirements for the Degree of  
Masters of Science in Aerospace Engineering**

**Embry-Riddle Aeronautical University  
Daytona Beach, Florida  
Spring 2011**

UMI Number: EP33517

All rights reserved

INFORMATION TO ALL USERS

The quality of this reproduction is dependent on the quality of the copy submitted.

In the unlikely event that the author did not send a complete manuscript and there are missing pages, these will be noted. Also, if material had to be removed, a note will indicate the deletion.



UMI EP33517

Copyright 2012 by ProQuest LLC.

All rights reserved. This edition of the work is protected against unauthorized copying under Title 17, United States Code.



ProQuest LLC.  
789 East Eisenhower Parkway  
P.O. Box 1346  
Ann Arbor, MI 48106 - 1346

HYDROSTATIC PRESSURE TESTING OF A SQUARE-CROSS SECTION  
STAINLESS STEEL PROPELLANT TANK MANUFACTURED USING  
SELECTIVE LASER SINTERING

By

Spencer Fuller

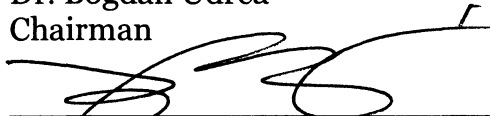
This thesis was prepared under the direction of the candidate's thesis committee chairman, Dr. Bogdan Udrea, Department of Aerospace Engineering, and has been approved by the members of his thesis committee. It was submitted to the Aerospace Engineering Department and was accepted in partial fulfillment of the requirements for the degree of Master of Science in Aerospace Engineering.

THESIS COMMITTEE:



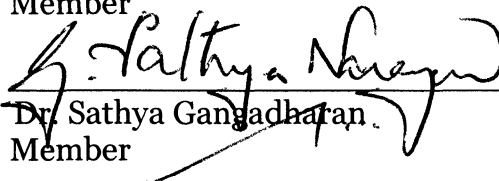
---

Dr. Bogdan Udrea  
Chairman



---

Dr. Yi Zhao  
Member



---

Dr. Sathya Gangadharan  
Member

*H. Narayanamanni / for Habib Eslami*

---

Dr. Habib Eslami  
Department Chair, Aerospace Engineering

*6/2/11*  
Date



---

Dr. Robert Oxley  
Associate Vice President for Academics

*6/2/11*  
Date

## **ACKNOWLEDGEMENTS**

The author wishes to express special thanks to the Thesis Chairman, Dr. Bogdan Udrea, whose encouragement, insight and practical suggestions were crucial to the successful completion of this thesis. Appreciation is also due to Mike Potash, Dr. Pat Anderson, Dr. Sathya Gangadhara, Dr. Jean-Michel Dhainaut, Mark Campere and Andy Snow for the use of testing equipment, construction of testing equipment or the manufacturing of the propellant tank.

This statement of acknowledgement would not be complete without a show of appreciation and gratitude to both the author's friends and family for providing the encouragement, stability and support needed to complete the task.

## **ABSTRACT**

**Author:** Spencer Fuller

**Title:** Hydrostatic Pressure Testing of a Square-Cross Section Stainless Steel Propellant Tank Manufactured Using Selective Laser Sintering

**Institution:** Embry-Riddle Aeronautical University

**Degree:** Master of Science in Aerospace Engineering

**Year:** 2011

The purpose of this study was to determine if parts manufactured using metal selective laser sintering (SLS) exhibit the same isotropic material properties as conventionally made metal parts. This was accomplished by performing a hydrostatic pressure test (HPT) of a metal SLS manufactured propellant tank, constructed for a nano-satellite of the cubesat class. Strain measurements from twelve strain gage locations on the propellant tank were recorded. A finite element analysis (FEA) model, which assumes isotropic material properties, was generated and a FEA analysis was ran at several pressure loads. The tanks strain data at the corresponding pressure loads from the HPT was then compared to the FEA data at the same pressure loads ranging from 500 to 3000psi. The two data sets were used for comparing material properties of the metal SLS and of the isotropic FEA model of the tank.

# TABLE OF CONTENTS

ACKNOWLEDGEMENTS.....	iii
ABSTRACT.....	iv
LIST OF TABLES .....	vii
LIST OF FIGURES.....	viii
INTRODUCTION.....	1
1.1    Review of Relevant Topics .....	1
1.2    Tank Design Progression .....	3
1.3    Selective Laser Sintering Tank Production.....	4
1.4    Research Motivation .....	7
METHOD OF TESTING .....	8
2.1    Hydrostatic Pressure Test Overview.....	8
2.2    Strain Gages Location Configuration and Installation.....	9
2.3    Strain Gage Bridge and Amplifier .....	11
2.4    Pressure Transducer .....	12
2.5    Data Acquisition Cards.....	13
2.6    LabVIEW .....	15
2.7    Calibration.....	18
2.8    Hydrostatic Pressure Test System .....	20

TEST RESULTS AND ANALYSIS.....	22
3.1 Propellant Tank Hydrostatic Pressure Test Results.....	22
3.2 Analysis.....	31
CONCLUSIONS .....	40
RECOMMENDATIONS.....	41
REFERENCES .....	42
APPENDIX.....	43



## LIST OF TABLES

Table 3-1. The EOS StrainlessSteel 17-4 material properties. ....	31
Table 3-2. The end-cap NASTRAN strain data. ....	35
Table 3-3. The end-cap strain data percent error. ....	37
Table 3-4. The vertical side wall NASTRAN data. ....	38
Table 3-5. The vertical strain gage percent error. ....	39

## LIST OF FIGURES

Figure 1-1. The dipping thermosphere explorer nanosatellite.....	1
Figure 1-2. ( <i>Left</i> ) The propellant tank and ( <i>Right</i> ) tank with cutout. ....	2
Figure 1-3. The first propellant tank design. ....	3
Figure 1-4. The final propellant tank using SLS. ....	4
Figure 1-5. A laser sintering machine schematic. ....	5
Figure 1-6. The post-processed tank STL file. ....	7
Figure 2-1. The test equipment setup diagram. ....	9
Figure 2-2. ( <i>Left</i> ) The strain gage location configuration and ( <i>Right</i> ) tank FEA displacements. ....	10
Figure 2-3. ( <i>Left</i> ) The tank after sanding preparation and ( <i>Right</i> ) wires are labeled. ....	11
Figure 2-4. The quarter-bridge strain gage configuration. ....	11
Figure 2-5. ( <i>Left</i> ) The quarter bridge/amp front and ( <i>Right</i> ) quarter bridge/amp back. ....	12
Figure 2-6. The Omegadyne PX41S0-30KG5V pressure transducer. ....	13
Figure 2-7. ( <i>Left</i> ) The NI PCI-6221 DAQ card and the ( <i>Right</i> ) NI USB-6008 DAQ card. ....	14
Figure 2-8. A SCB-68 terminal board block. ....	15
Figure 2-9. The graphic user interface for 13 data channels. ....	16
Figure 2-10. The virtual instruments block diagram. ....	17

Figure 2-11. The strain channel configuration screen.....	18
Figure 2-12. ( <i>Left and Right</i> ) Calibration Beam Test Setup .....	19
Figure 2-13. The Vishay P-3500 Strain Indicator. ....	20
Figure 2-14. A schematic of the HPT system. ....	20
Figure 2-15. The HPT system. ....	21
Figure 2-16. The HPT test Section chamber. ....	21
Figure 3-1. The tank internal pressure during testing. ....	23
Figure 3-2. Von Mises stresses of the baffle.....	23
Figure 3-3. Close up of a baffle hole Von Mises stress.....	24
Figure 3-4. The baffle and center post failure.....	25
Figure 3-5. ( <i>Left and Right</i> ) The propellant tank after rupture.....	25
Figure 3-6. ( <i>Left and Right</i> ) Tank Rupture Placement .....	26
Figure 3-7. The graph of ( <i>Top</i> ) pressure and ( <i>Bottom</i> ) Channel 2 and 8. ....	27
Figure 3-8. The graph of ( <i>Top</i> ) pressure and ( <i>Bottom</i> ) channels 1 and 7.....	28
Figure 3-9. The graph for ( <i>Top</i> ) Pressure and ( <i>Bottom</i> ) Channels 4 and 10.....	29
Figure 3-10. The graph for ( <i>Top</i> ) pressure ( <i>Bottom</i> ) channels 5 and 11 .....	29
Figure 3-11. The graph for ( <i>Top</i> ) pressure, ( <i>Middle</i> ) channel 3 and ( <i>Bottom</i> ) channel 6. ....	30
Figure 3-12. The graph for ( <i>Top</i> ) pressure, ( <i>Middle</i> ) channel 9 and ( <i>Bottom</i> ) channel 12.....	31
Figure 3-13. An example of the end-cap tetrahedron selection.....	34
Figure 3-14. The end-cap sample median pressure value and distribution. ....	36

Figure 3-15. The vertical side wall sample median pressure and distribution..... 39

# INTRODUCTION

## 1.1 Review of Relevant Topics

During the 2008-2009 academic year section 02 of the Spacecraft Design course (AE427/445) designed a 3U cubesat for the National Science Foundation program *CubeSat-based Science Missions for Space Weather and Atmospheric Research* (NSF 09-523). This mission had been named the *Dipping Thermosphere Explorer*, or DipTE for short and the overall design is shown in Figure 1-1. The proposed DipTE design had included a propulsion system for both orbital maneuvering and reaction control of the attitude.

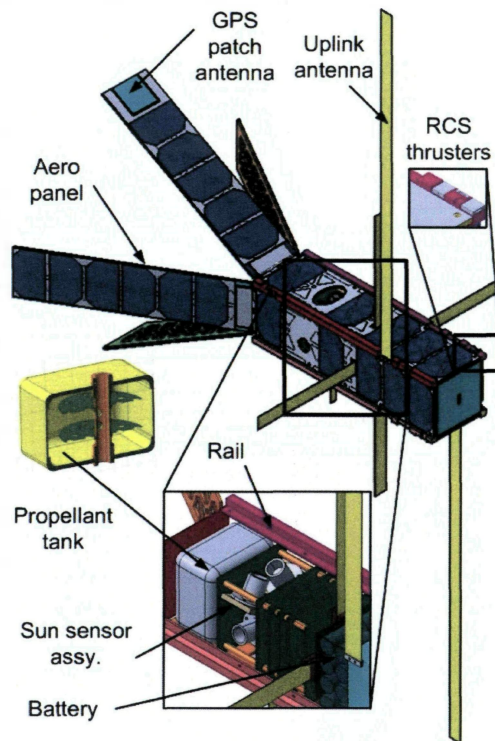


Figure 1-1. The dipping thermosphere explorer nanosatellite.

The propellant tank for the propulsion system can also be seen in Figure 1-1. The tank is designed to hold a target absolute pressure of 1300psi, which includes a factor of safety of 1.5. The tank has an internal volume of approximately 18in<sup>3</sup>. An internal baffle is included in the tank design to prevent sloshing of propellant during orbital maneuvers or other satellite movements. A center post in the tank design allows for the filling and purging of the propellant tank as well as giving a mounting surface for the baffle and additional structural support. Most pressure vessels have a circular cross-section and hemispherical end-caps because these shapes allow for easy stress analysis and relatively simple construction. The main design driver for the propellant tank is to maximize its internal volume and as a consequence it is designed using a square cross-section. The outside of the tank as well as a cutout showing the tanks internal center post and baffle is seen in Figure 1-2.

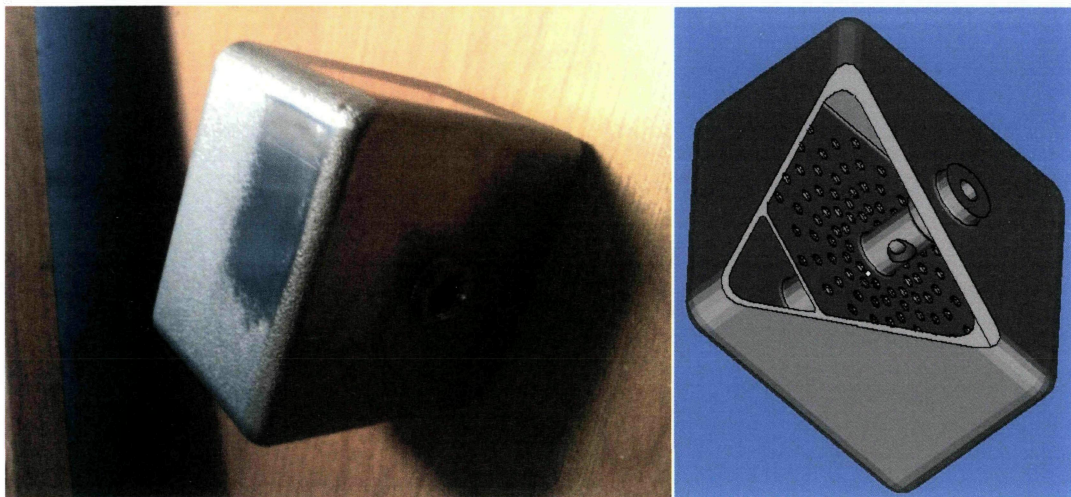


Figure 1-2. (*Left*) The propellant tank and (*Right*) tank with cutout.

## 1.2 Tank Design Progression

During the initial design, conventional manufacturing methods are envisioned when making design decision for tank. The first propellant tank design, shown in Figure 1-3, is manufactured from several separate parts, which are assembled and welded together. The cost, time and skilled labor that it would take to manufacture each tank part and then weld them together is prohibitive.

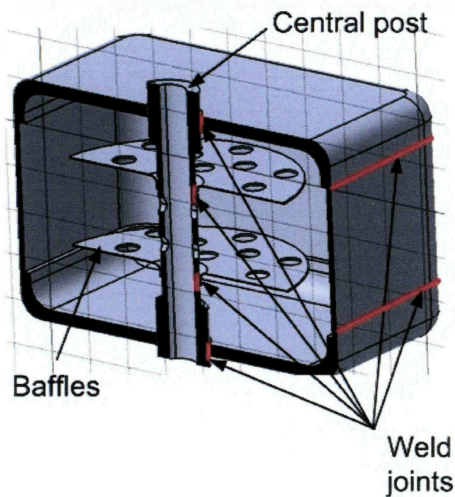


Figure 1-3. The first propellant tank design.

Consequently, the tank is redesigned with selective laser sintering (SLS) manufacturing methods in mind. SLS is an additive manufacturing method and is explained in more detail in Section 1.3. SLS manufacturing allows the tank to be fabricated without any welding or separate part creation. The new design, which takes advantage of the SLS manufacturing by extending the single baffle all the way to the tank walls for additional structural support, is shown in Figure 1-4.

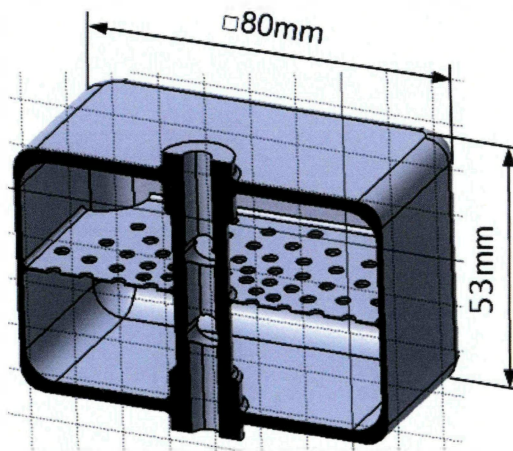


Figure 1-4. The final propellant tank using SLS.

### **1.3 Selective Laser Sintering Tank Production**

A SLS machine builds-up layers by the local melting of a powder of each layer. The powder is deposited in a thin layer by a spreader mechanism, with the first layer deposited on the top of a build platform. A scanning mechanism steers a laser beam to trace the shape of a "slice" of the part on the fresh powder and selectively melting it. The melted material fuses to its surroundings once it cools down. After each new layer is produced, the build platform is lowered and the spreader deposits a new layer of powder on top of the previous one. A schematic of a laser sintering machine is shown in Figure 1-5.



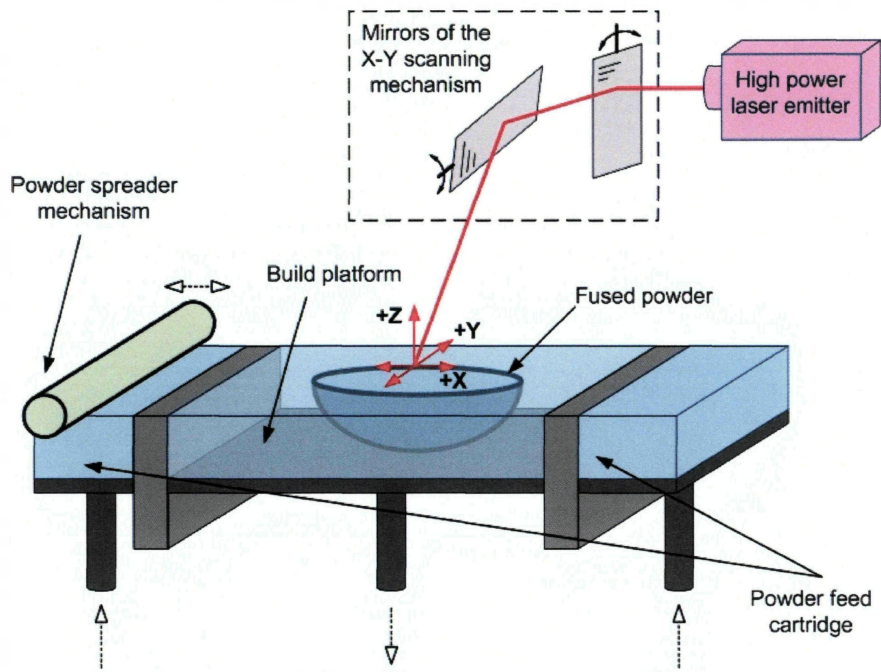


Figure 1-5. A laser sintering machine schematic.

Fabricating a part on a SLS machine starts with the designing the part in a solid modeling software program, such as CATIA or Solidworks. The solid model created is then exported as a stereo-lithography (STL) file. The next step is to post-process the STL file using a specialized application that has modules for the designing of support structures for the parts being created, for calculating the quantity of powder required and the time needed to fabricate the part. Then the STL file is cut into layers by the post-processing software and generates the path of the laser beam for the SLS machine. After the fabrication cycle has ended the fused metal will be surrounded by the unused unfused metal powder. At the end of a cool down period the fused metal is removed from the surrounding unfused metal and placed on a cool down rack and allowed to fully cool to room temperature. Then any support structures that were created by the post-processing software are removed and discarded. Any powder still attached to the

part or left in internal cavities is removed using tools such as scraping knives, brushes, and air blowers. After all of the unfused powder is removed the part can be polished, threaded, shot peened or even heat treated just like conventionally made parts.

The propellant tank is manufactured on an Electro Optical Systems (EOS) M270 SLS machine using EOS StrainlessSteel 17-4. The effective building volume of the EOS M270 is 250 x 250 x 215mm which is almost four times the longest dimension of the propellant tank allowing more than enough room to construct the propellant tank [1]. After the propellant tanks STL file is generated and sent to EOS the application engineer post-processes it for fabrication on the M270 machine. The post-processed file with support structures, added in red, can be seen in Figure 1-6. The tank is canted in order to provide good stability for the thin walls while being constructed. The added support structures are cut off after construction is completed and the exposed surfaces are sanded create relatively uniform surfaces. The unfused metal powder within the tank is removed using pressurized air.



Figure 1-6. The post-processed tank STL file.

## 1.4 Research Motivation

Due to the layered construction of SLS manufacturing conventional wisdom suggests that SLS parts may not have isotropic material properties. According to [2] the material properties of plastic SLS parts are 70 to 80 percent that of molded plastic parts however this may not be the case for metal SLS parts. Aerospace and medical companies that commonly use metal SLS parts have performed material properties tests in order to certify many SLS parts. According to [2] the results are confidential, but point to "very similar" ultimate tensile strength, yield strength, and elongation to parts fabricated from wrought metal and "better than casting in many cases." These claims suggest that when tested the metal SLS propellant tank will perform the same as a tank constructed by conventional means.

## **METHOD OF TESTING**

### **2.1 Hydrostatic Pressure Test Overview**

The best choice to test the material properties of the propellant tank is a hydrostatic pressure test given that it is after all designed to be a pressure vessel. The hydrostatic pressure chamber and hydrostatic pressure system at Embry-Riddle's Structures Lab has been successfully used in the past for Icarus rocket engine testing. Strain gages are bonded at strategic locations, shown in Figure 2-2, on the surface of the propellant tank to gather strain readings during the hydrostatic pressure test (HPT). During the HPT each strain gauge is arranged in a quarter-bridge configuration and attached to a 1000 gain amplifier. Each strain gauge channel is fed into a data acquisition (DAQ) card so the signal can be input into a computer then read, displayed and recorded by a National Instruments LabVIEW script. The data from a pressure transducer is also fed into a DAQ card so that each time the pressure is read, displayed and recorded it can be directly correlated to each strain gage channel for that particular sampling. The entire test equipment step-up diagram can be seen in Figure 2-1.

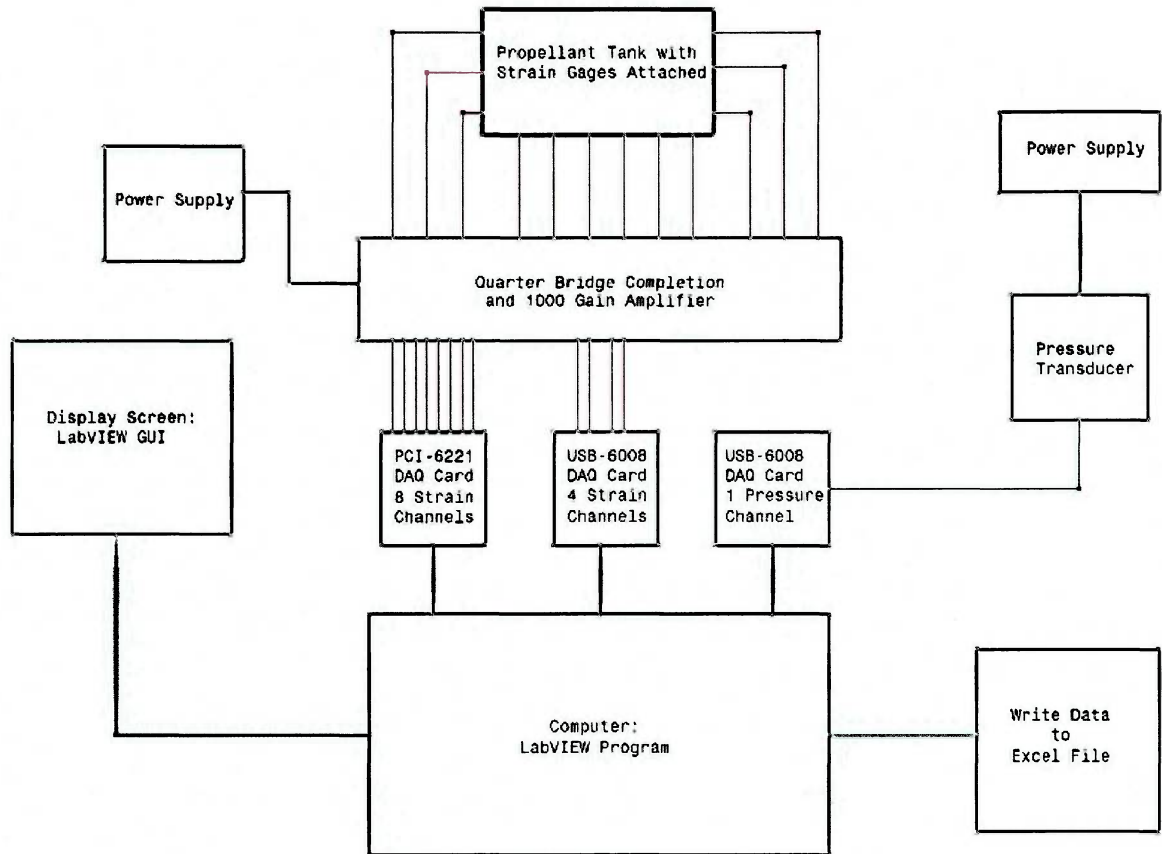


Figure 2-1. The test equipment setup diagram.

## 2.2 Strain Gages Location Configuration and Installation

The strain gages in the quarter-bridge configuration are the  $350\Omega \pm 0.3\%$  Micro-Measurements model number CEA-06-250UW-35 [3]. This particular model is made for bonding to steel and with an area of  $0.1485\text{in}^2$  it can easily be applied to the relatively small surface area of the tank with room to spare. The strain gages are placed on the surface of the propellant tank at locations that have relatively large deformations while pressurized and thus large strain determined by inspecting the Finite Element Analysis (FEA) performed on the tank using FEMAP and NASTRAN FEA software prior to testing. The strain gage locations are numbered with a clockwise numbering convention, which can be seen in

Figure 2-2. A sample of the FEA used to determine these locations can also be seen in Figure 2-2. The six strain gages shown in Figure 2-2 are mirrored on the opposite bottom corner for a total of twelve strain gages giving the test a redundant set of strain gages.

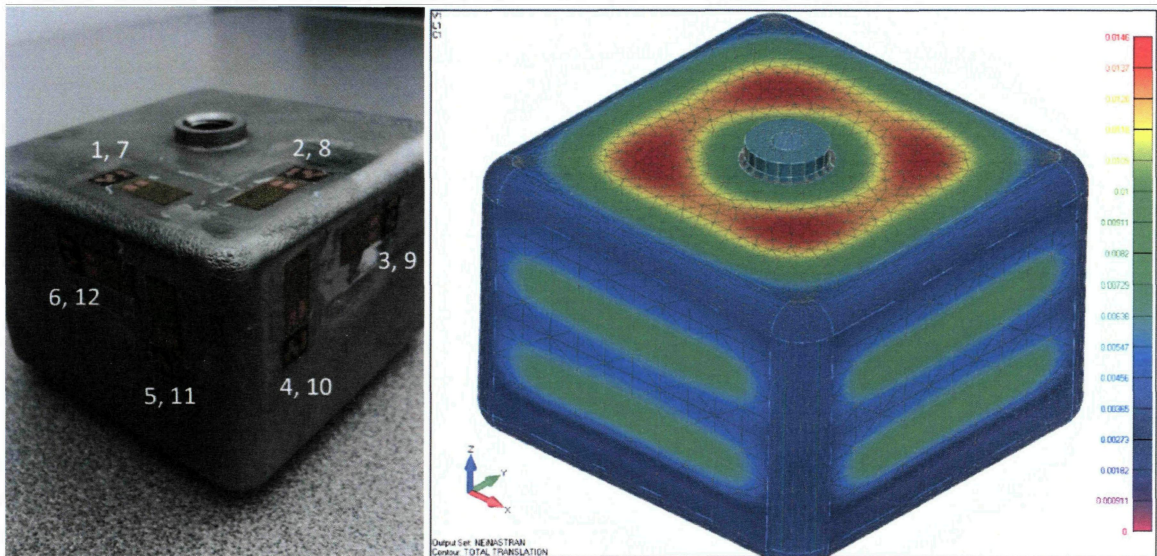


Figure 2-2. (Left) The strain gage location configuration and (Right) tank FEA displacements.

The strain gages are attached to the tank using recommended bonding instructions found on the micro-measurements website [4]. Initially the tanks surfaces are too rough for the strain gages to be bonded so they are sanded down to smoother surfaces, which can be seen in Figure 2-3. The strain gages and stress relief bonding terminals are bonded to the surface of the tank, the three-wire quarter-bridge setup are soldered to each gage and relief terminal. Each channel is labeled to insure that there is no confusion between which channels belonged to which strain gages; the result can be seen in Figure 2-3.

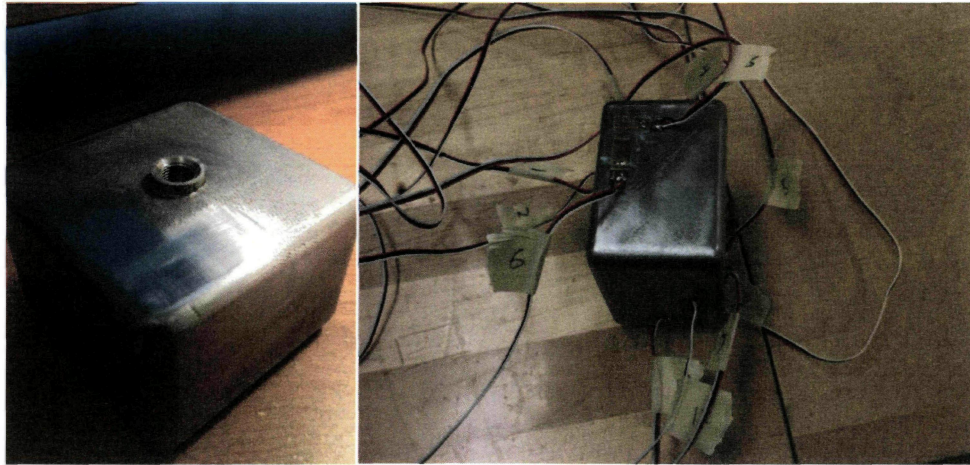


Figure 2-3. (Left) The tank after sanding preparation and (Right) wires are labeled.

### 2.3 Strain Gage Bridge and Amplifier

Mike Potash, an ERAU Electronics Technician, created a quarter-bridge and amplifier for each one of the strain gage channels. This is accomplished, for each channel, by using three  $350\Omega$  resistors ( $R_1$ ,  $R_2$ , and  $R_3$ ) along with the  $350\Omega$  strain gage ( $R_G$ ) in a three wire quarter-bridge configuration as seen in Figure 2-4.

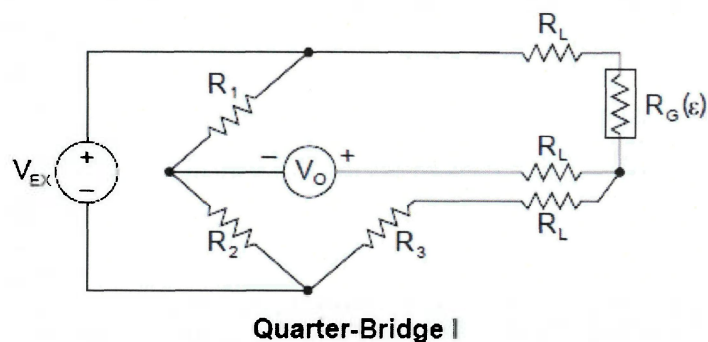


Figure 2-4. The quarter-bridge strain gage configuration.

An excitation voltage ( $V_{EX}$ ) of 8.19 VDC is applied to the quarter-bridge for each channel. The lead resistance ( $R_L$ ) is measured before the test and is determined

to be  $0.40\Omega$ . The output of each one of the quarter bridges is applied to a 1000 gain amplifier. For the strain gages used the gage factor, used in the strain gage equation to calculate strain in Section 2.6, is  $2.11 \pm 0.5\%$  at  $75^\circ\text{F}$  [3]. A potentiometer on each channel allows the balancing of each channel before testing because an unstrained strain gage should have zero voltage. These balancing potentiometers can be seen in Figure 2-5. Balancing was performed, for each channel, right before testing the tank and after all wires and equipment were in their final positions. Figure 2-5 shows some of the internal components of the quarter bridges and amplifiers as the labeled strain gage input wire connections.

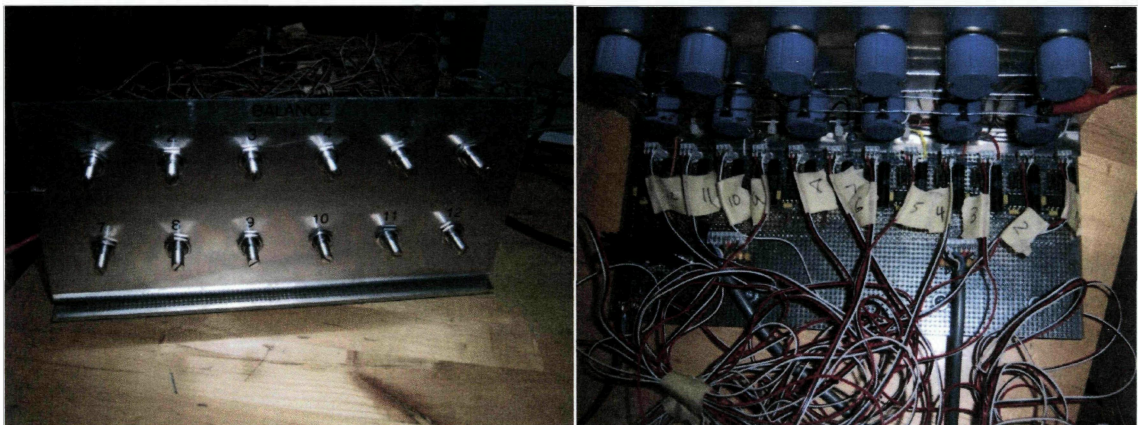


Figure 2-5. (*Left*) The quarter bridge/amp front and (*Right*) quarter bridge/amp back.

## 2.4 Pressure Transducer

An Omegadyne PX41S0-30KG5V pressure transducer is used so the tanks internal pressure can be compared to each strain gage channel at any point during the test and is shown in Figure 2-6. The pressure transducer requires an excitation voltage range of 10 to 40 VDC, has an output range of 0.5 to 5.5 VDC



and can measure pressure from 0 to 30,000 psi which are all well within the range of the test [5].



Figure 2-6. The Omegadyne PX41S0-30KG5V pressure transducer.

A BK Precision model 1670A power supply is used to apply an excitation voltage of 28 Volts DC to the pressure transducer during testing. The output of the pressure transducer is connected to a DAQ card as the 13<sup>th</sup> channel and recorded along with the twelve strain channels.

## 2.5 Data Acquisition Cards

Three DAQ cards are used during the pressure test to accommodate the 13 differentially measured channels. One NI PCI-6221 DAQ card and one NI USB-6008 DAQ card are used to acquire the data from the 12 strain gage channels. The NI PCI-6221 DAQ, shown in Figure 2-7, card is used for the strain channels 1 through 8 because that particular card has 8 differentially measured inputs. The NI USB-6008, shown in Figure 2-7, only has four differentially measured inputs so it is used for strain channels 9 through 12. The third DAQ card, another NI USB-6008, is used to acquire the last channel, which is the pressure or channel

13. All of these cards have an input range of  $\pm 10$  VDC [6] and the information gather by each card is fed into LabVIEW for further use.

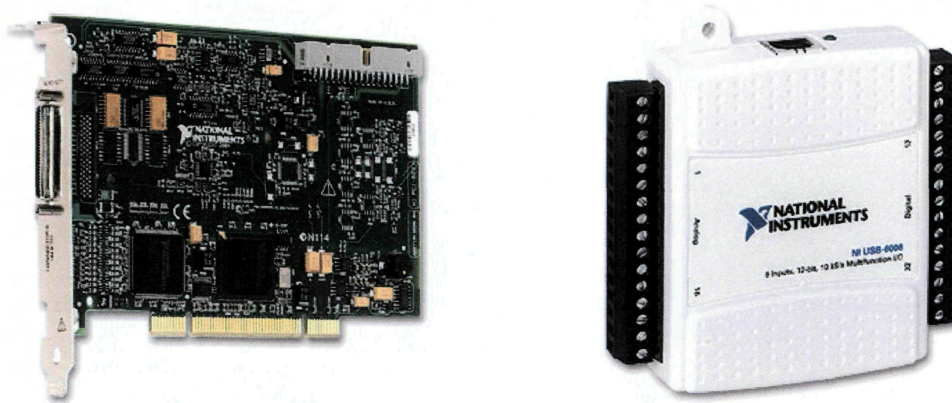


Figure 2-7. (Left) The NI PCI-6221 DAQ card and the (Right) NI USB-6008 DAQ card.

Channels 9 through 12 are connected to the input of the NI USB-6008 using its built in terminal boards. Using a USB connector the NI USB-6008 DAQ cards output is input into a PC so the data can be obtained. The NI PCI-6221 DAQ card requires an additional SCB-68 terminal board block since it has no built-in terminal board because it is installed inside a PCI slot of the PC. The SCB-68, shown in Figure 2-8, is connected to the NI PCI-6221 DAQ card using a serial connector.

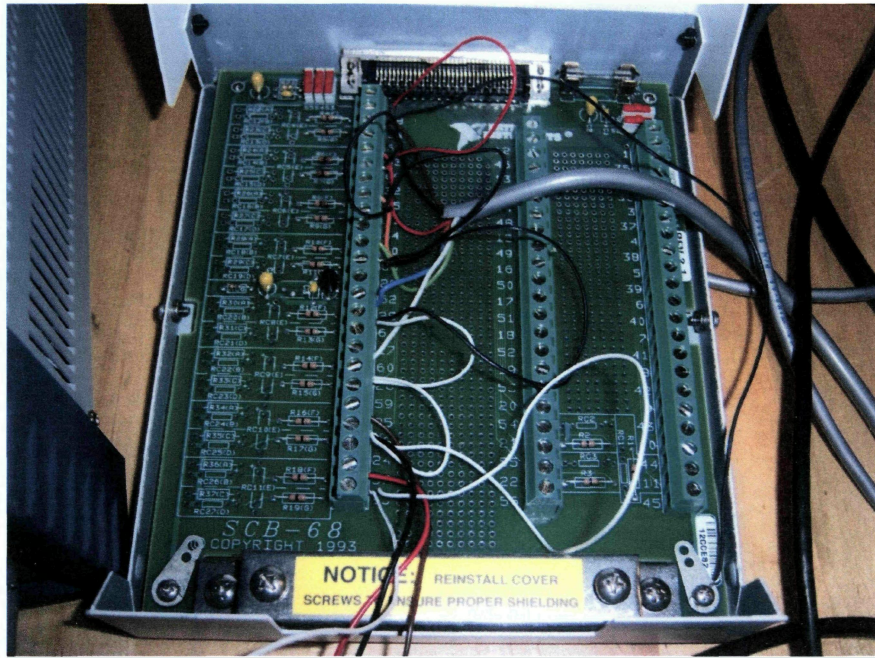


Figure 2-8. A SCB-68 terminal board block.

## 2.6 LabVIEW

The data input from the DAQ cards to the PC needed some type of software so the data can be displayed, recorded, isolated or processed as needed. National Instrument's LabVIEW is a good choice for this software since it is design to work with the DAQ cards that are used. A program is written in LabVIEW to display, in real time, all 12 of the strain channels along with the 13th pressure channel. This is accomplished by writing a virtual instrument (VI) that displays the strain and pressure data in a graphic user interface (GUI). In this particular case, the GUI used to display the test data is 13 waveform graphs that are shown in Figure 2-9.

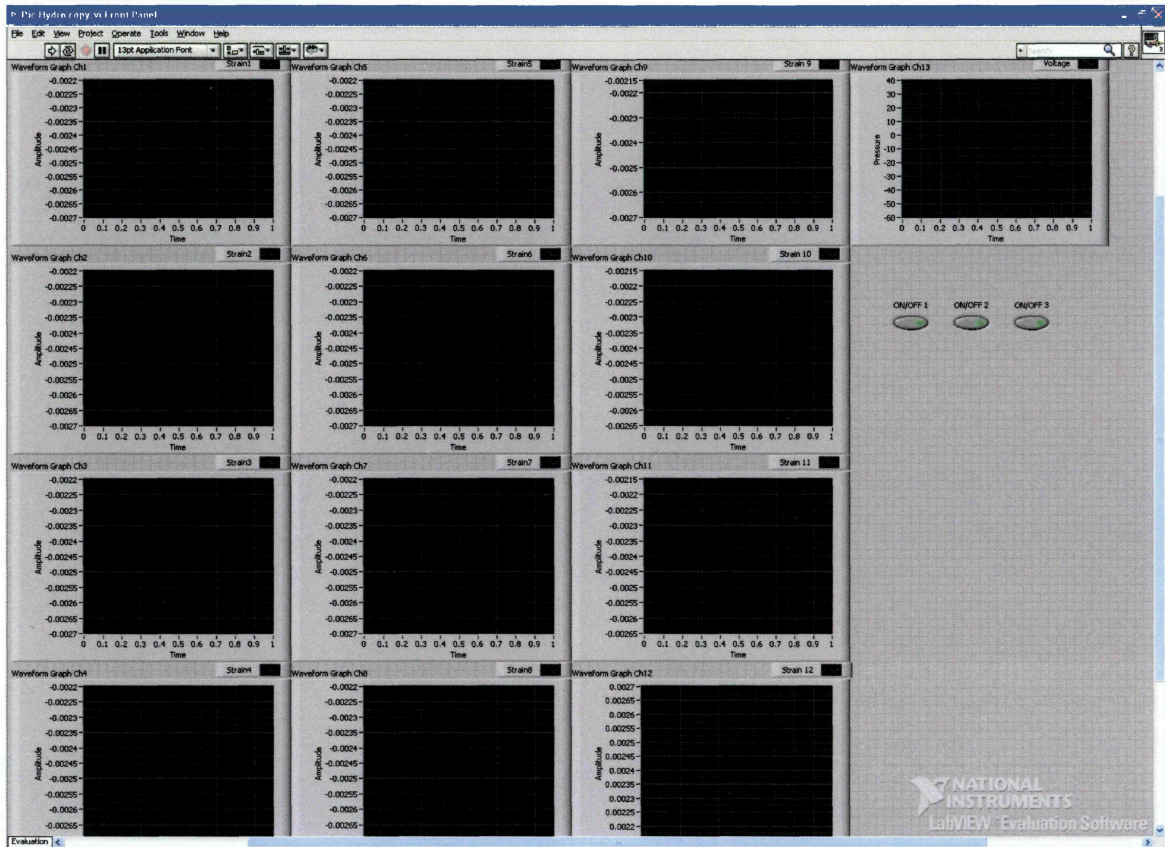


Figure 2-9. The graphic user interface for 13 data channels.

The VI also programmed to save the data from all 13 test channels to a file so the data can be used later for analysis. This is accomplished by including a "Write to Measurement File" block in the VI's code, which can be seen along with the entire VI's block diagram code in Figure 2-10. Since three "Write to Measurement File" blocks are used, one for each DAQ used, they are set up so they each have a time column to go along with the data channels columns so that data from all three files can be synchronized.

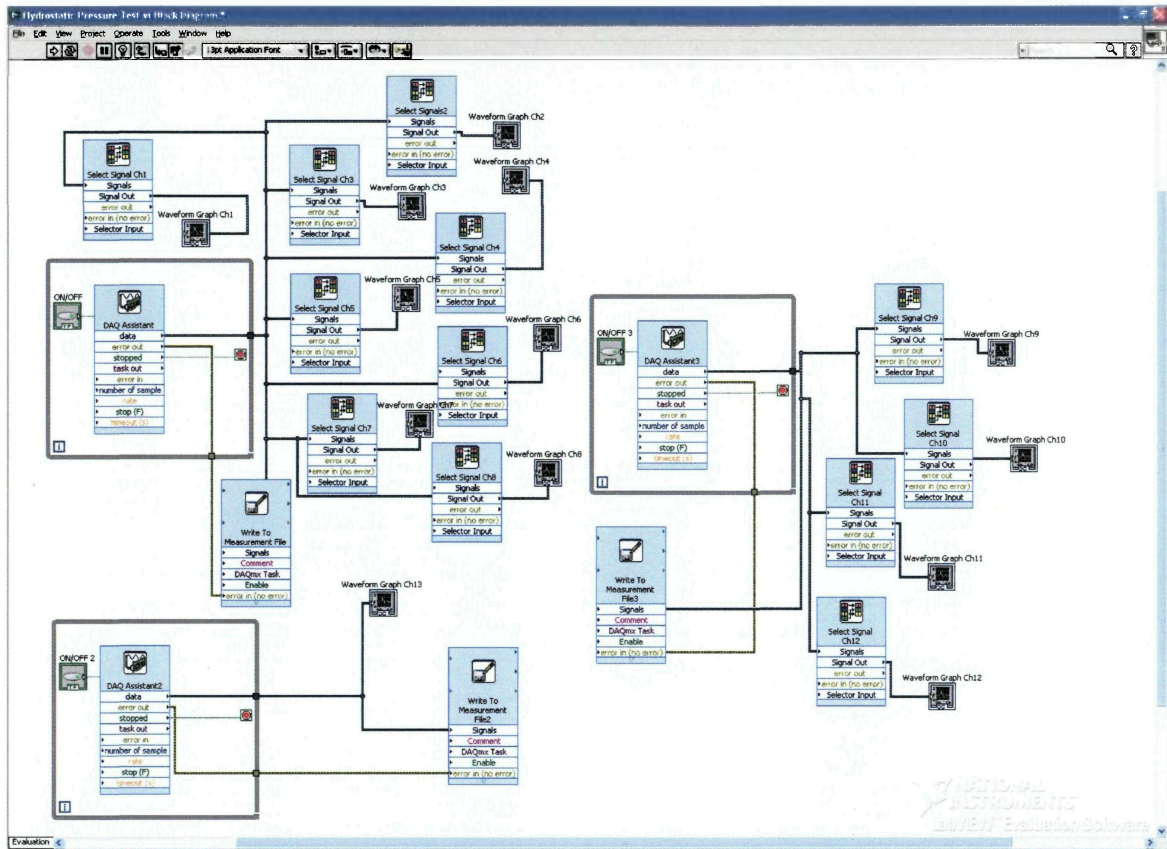


Figure 2-10. The virtual instruments block diagram.

It is necessary to use Equations 1 and 2 to determine the strain from the output voltage reading from the quarter-bridge strain gage setup if done manually.

$$V_r = \frac{V_{output(strained)} - V_{output(unstrained)}}{V_{excitation after gain}} \quad \text{Eq. 1}$$

$$\epsilon (strain) = \frac{-4V_r}{GageFactor(1 + 2V_r)} \cdot \left(1 + \frac{R_{Lead wires}}{R_{Gage}}\right) \quad \text{Eq. 2}$$

LabVIEW will calculate strain automatically when all of the appropriate information is input into the strain channel configuration screen seen in Figure

2-11. For this test all the information is known from the manufactures specifications or from direct measurement before the test, which allows the strain channels to display actual strain values and be monitored in real time.

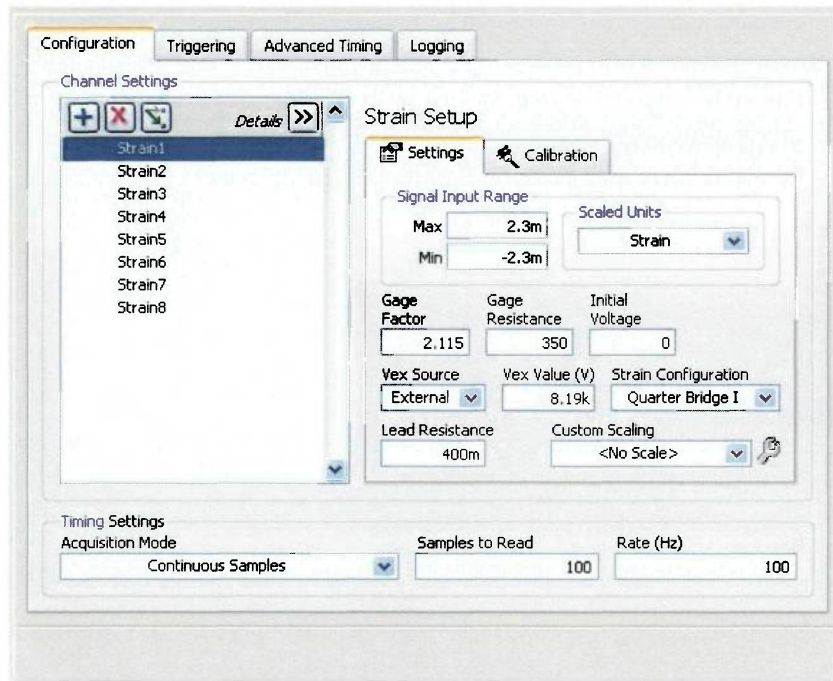


Figure 2-11. The strain channel configuration screen

## 2.7 Calibration

To insure that the strain gages and entire data acquisition system is performing properly, a calibration test is done prior to any tank testing. This calibration test is accomplished by clamping a long slender beam to a table and bonding a strain gage close to the edge of the table as seen in Figure 2-12.

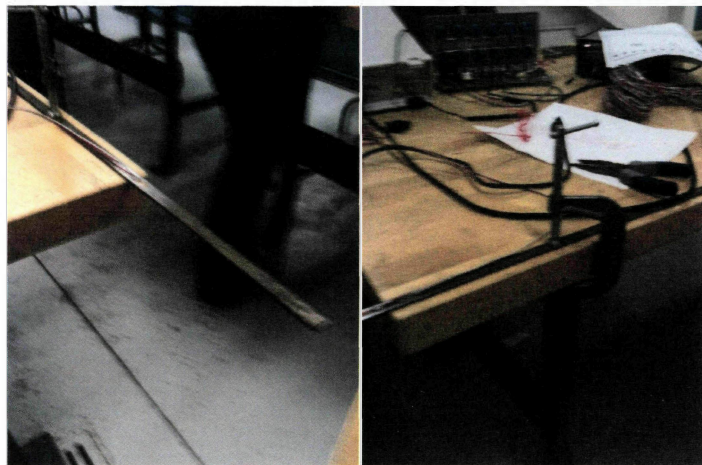


Figure 2-12. (*Left and Right*) Calibration Beam Test Setup

The beam is loaded with a calibrated weight of 1kg which is attached 0.5in from the free end of the beam. The strain gage connections are attached to a Vishay P-3500 Strain Indicator, seen in Figure 2-13, and the strain value are read and recorded, this process is repeated with 2kg and 3kg calibrated weights. The P-3500 Strain Indicator is considered a high precision measurement device, so a transfer standard can be used and the results considered true known values of strain for the setup. The strain gage connections are connected to one of the DAQ card inputs and the strain values measured in LabVIEW are recorded. The known values are then compared to the LabVIEW values and found to be within less than 1% of each other so the system is determined to be setup and calibrated correctly.



Figure 2-13. The Vishay P-3500 Strain Indicator.

## 2.8 Hydrostatic Pressure Test System

The HPT uses a pneumatic driven piston pump with two check valves to prevent back flow. The pump operates on 10-100psi air pressure input which also controls the output. The pump will output up to 18,500psi with 100psi air pressure input. A basic schematic of the HPT system can be seen in Figure 2-14. The HPT system is located inside a full enclosed steel test Section to prevent damage and injury during testing. The pressure system and the outside of the test Section is shown in Figure 2-15 and Figure 2-16 respectively.

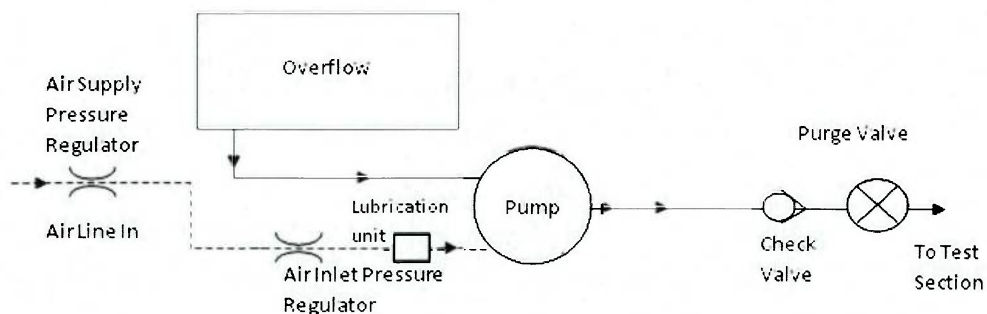


Figure 2-14. A schematic of the HPT system.



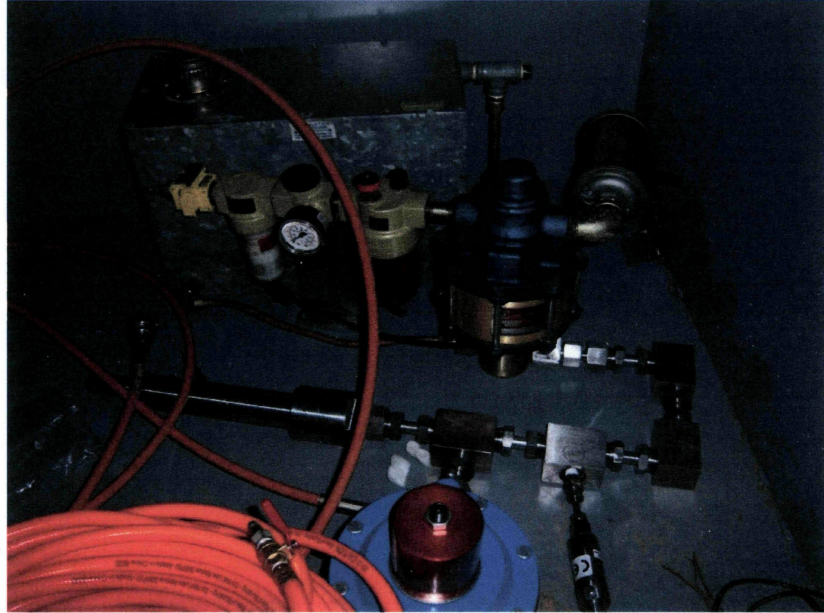


Figure 2-15. The HPT system.



Figure 2-16. The HPT test Section chamber.

## TEST RESULTS AND ANALYSIS

### 3.1 Propellant Tank Hydrostatic Pressure Test Results

Examination of Figure 3-1 shows that pressure in the tank dropped significantly four times during the HPT. The pressure drops correspond to failures of the internal structural supports of the tank, i.e. the baffle and center post. The failed internal supports are shown in Figure 3-4. The first pressure drop at 3700psi is most likely due to the failure of the baffle in one of the directions in the plane of the baffle allowing two of the side walls to rapidly expand. The baffles Von Mises stresses are shown in Figure 3-2 which include the maximum stress of the entire tank further supports the theory that the baffle is location of the failure. A close up of the maximum Von Mises stress is shown in Figure 3-3. The second pressure drop at approximately 4200psi is most likely due to the baffle failing in the other direction in the plane of the baffle allowing the other two side walls to expand rapidly. The third pressure drop at approximately 4000psi is mostly due to failure of the center post allowing the end-caps to rapidly expand. The final pressure drop at approximately 4700psi is due to the tank rupture seen in Figure 3-5.

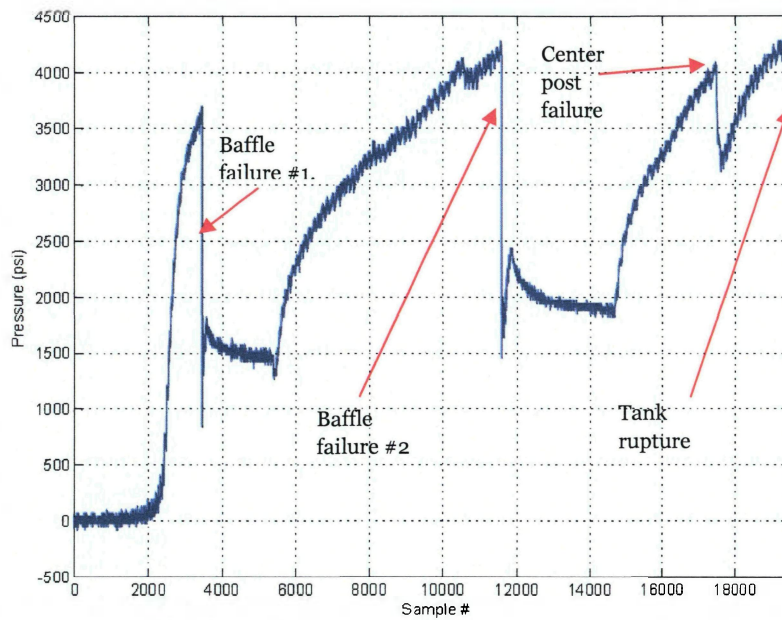


Figure 3-1. The tank internal pressure during testing.

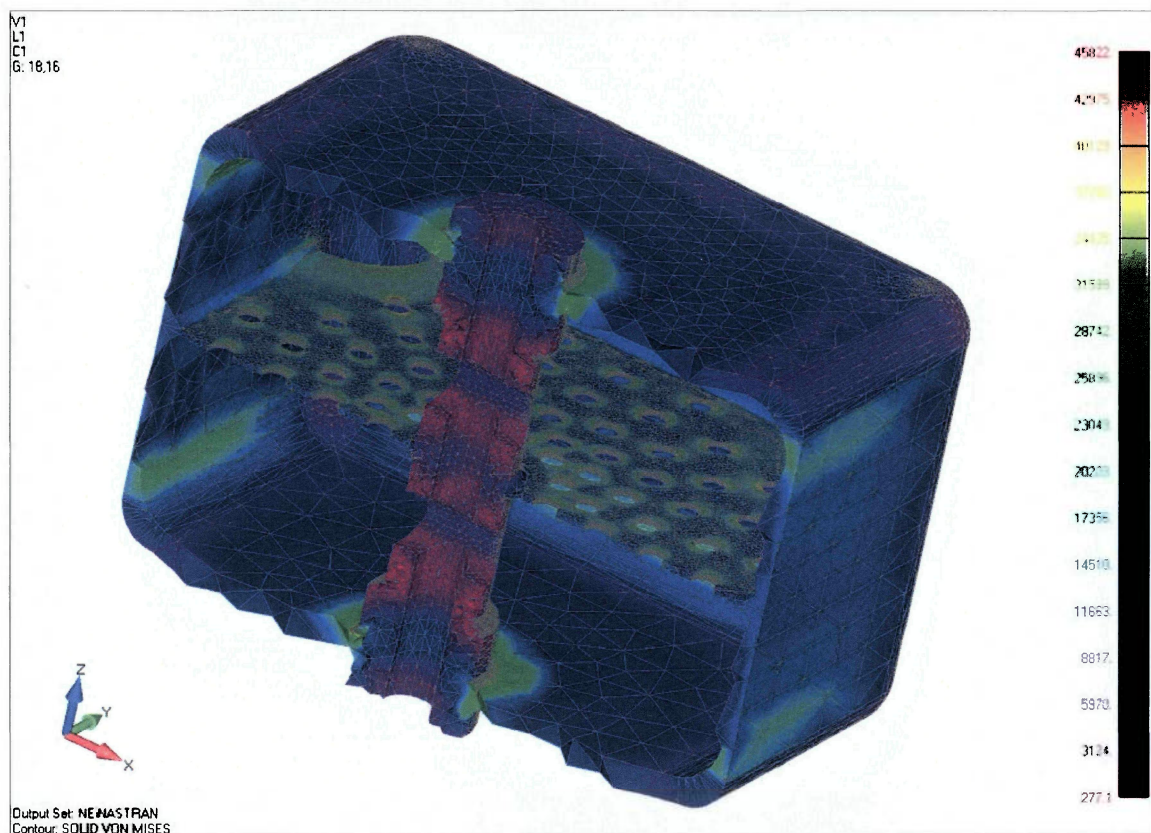


Figure 3-2. Von Mises stresses of the baffle.

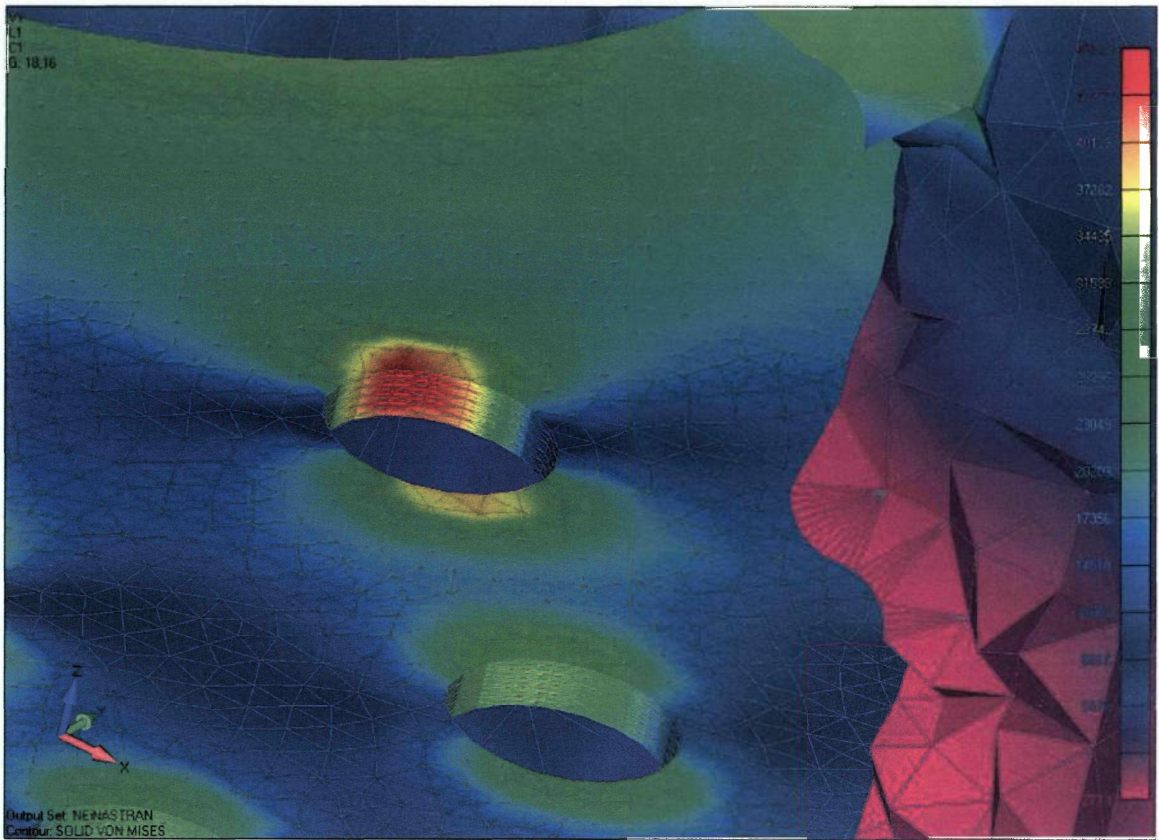


Figure 3-3. Close up of a baffle hole Von Mises stress.



Figure 3-4. The baffle and center post failure.

Only the data collected before the initial failure has been used for analysis in Section 3.2. The ruptured tank is shown in seen in Figure 3-5.

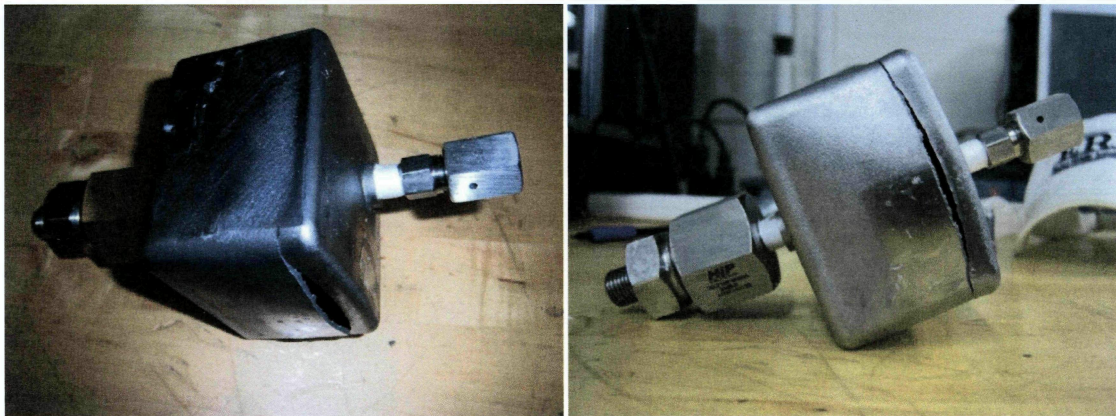


Figure 3-5. (Left and Right) The propellant tank after rupture.

The tank rupture occurred in virtually a straight line next to one of the thicker edges as shown in Figure 3-6. The tank wall is a thin plate with a uniformly distributed load with fixed boundary conditions on all edges. Theory predicts that the highest stresses are located along the boundary and it is most likely that the rupture will occur in this region. This is not necessarily expected for anisotropic materials that are created in layers like the propellant tank. If the material properties are different in the direction perpendicular to the building layer plane it might be expected that the rupture will occur along the edge of one of the build layers. This does not prove that the tank is or is not isotropic but it is of note.

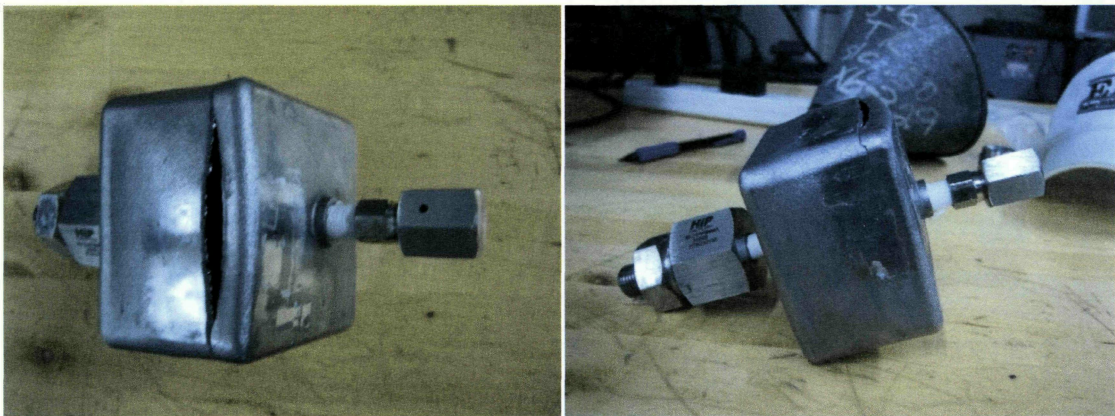


Figure 3-6. (*Left and Right*) Tank Rupture Placement

Since the strain data from each channel is recorded during the HPT, they can be compared to one another as well as NASTRAN data. The tank is symmetric about all three axes so channels 7 and 8 are mirrors opposites of channels 1 and 2. This means that channels 1 and 7 should be closely related as should channels 2 and 8. These gage relations are shown in Figure 2-2. The strain measured by

channel 8 confirms the symmetry assumption as shown in Figure 3-7. However, channel 7, seen in Figure 3-8, does not show any strain until the tank is pressurized to around 2000psi which does not match channel 1 or any other end-cap channels at all. This discrepancy could be due to less than optimal strain gage location, insufficient bonding or even hardware failure within the channel. Since this data does not correspond with the other end-cap channels, it will not be used in the analysis in Section 3.2. Figure 3-7 also shows that when the failure occurs at approximately 3700psi the strain in channel 2 rises while the strain in channel 8 falls by roughly the same amount. This is most likely due to one end-cap expanding relieving some of the pressure on the other end-cap allowing it to contract.

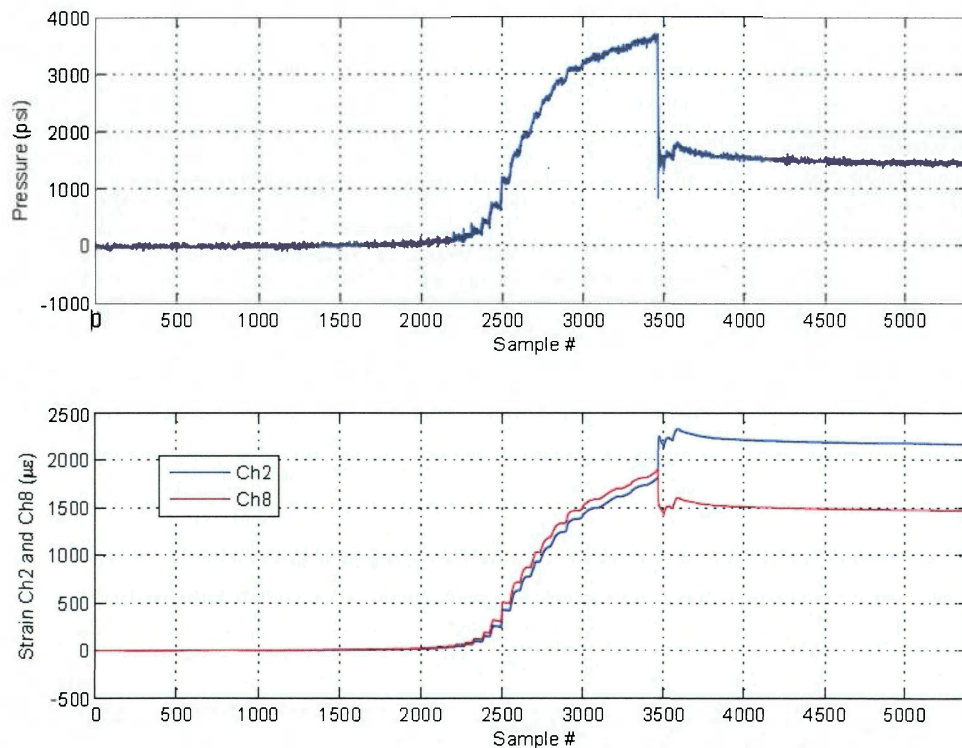


Figure 3-7. The graph of (*Top*) pressure and (*Bottom*) Channel 2 and 8.

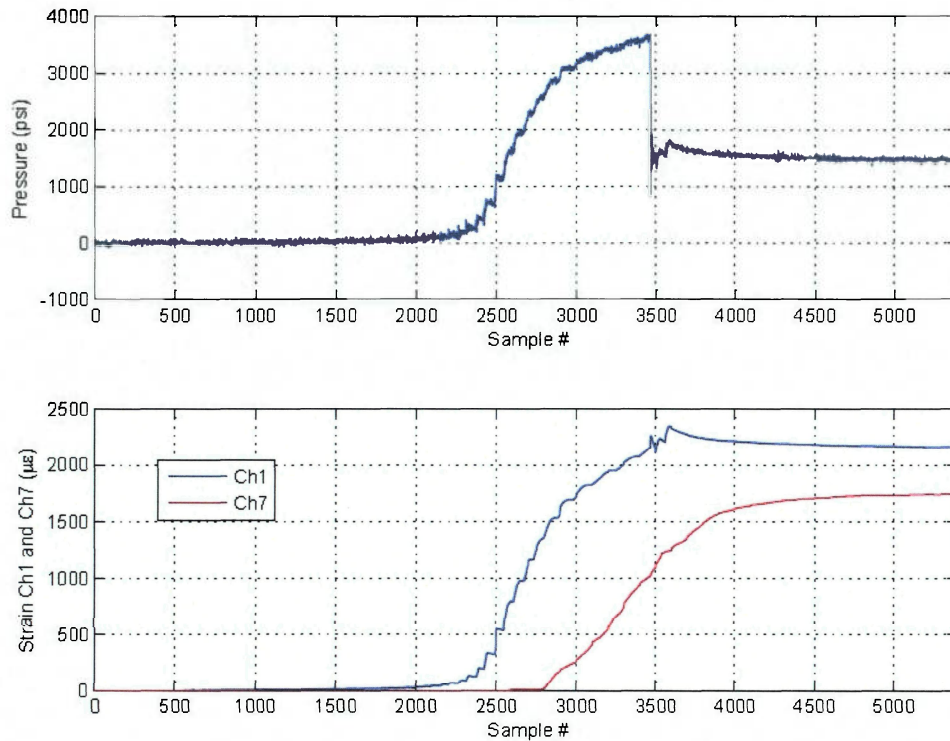


Figure 3-8. The graph of (Top) pressure and (Bottom) channels 1 and 7.

The vertical sidewall strain channels 4 and 10 and 5 and 11 can be seen in Figure 3-9 and Figure 3-10 respectively. They show that channels 5 and 11 are very similar, which again is expected since they are placed in location that are mirror opposites on one another. However, channels 4 and 10 are not similar even though they are opposites. This most likely is due to less than optimal strain gage placement or inadequate bonding to one or both gages.



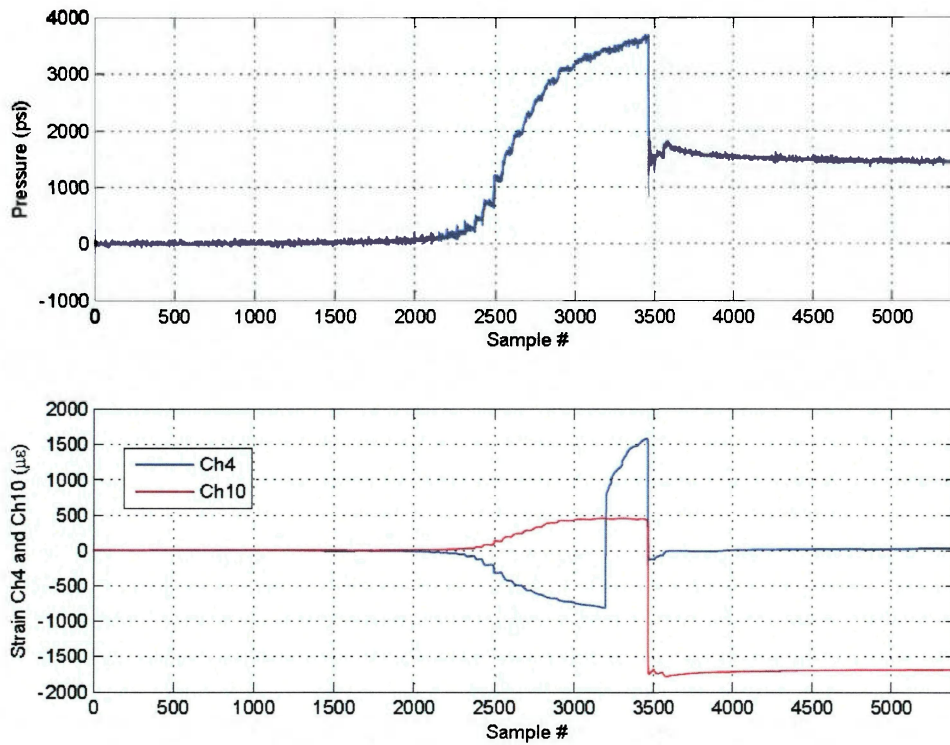


Figure 3-9. The graph for (Top) Pressure and (Bottom) Channels 4 and 10

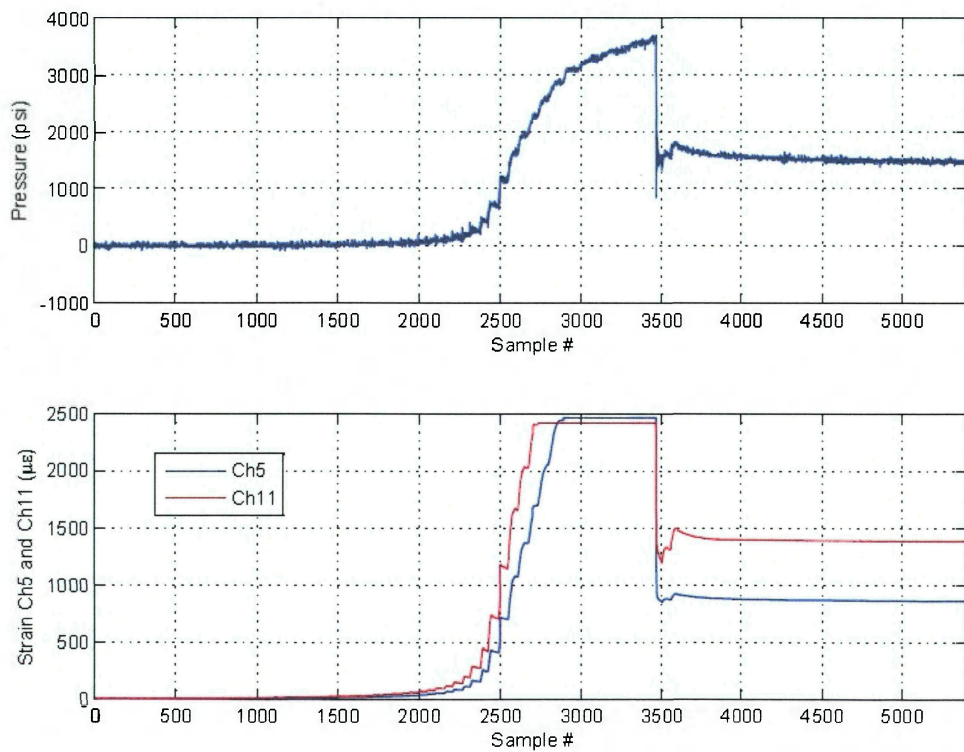


Figure 3-10. The graph for (Top) pressure (Bottom) channels 5 and 11

The horizontal sidewall strain channels 3 and 6 and 9 and 12, Shown in Figure 3-11 and Figure 3-12 respectively, do not show much strain until failure occurs. This is mostly likely due to the baffle breaking and allowing the tank walls to expand suddenly. In addition, each channel has a different graph shape even though they should be similar. This is most likely because the horizontal strain gage locations were too close to the edge of the tank so the gages were in areas with low strain on the axis measured, in this case the y axis. This allowed small changes in strain and strain gage locations to show very different graphs. For these reasons, the horizontal strain gage channels will not be used for analysis in Section 3.2.

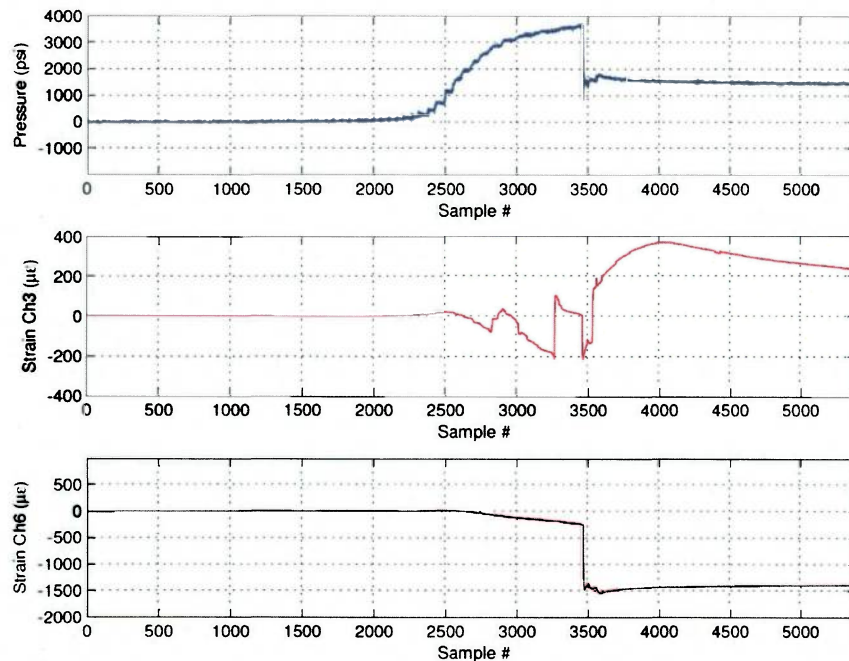


Figure 3-11. The graph for (Top) pressure, (Middle) channel 3 and (Bottom) channel 6.

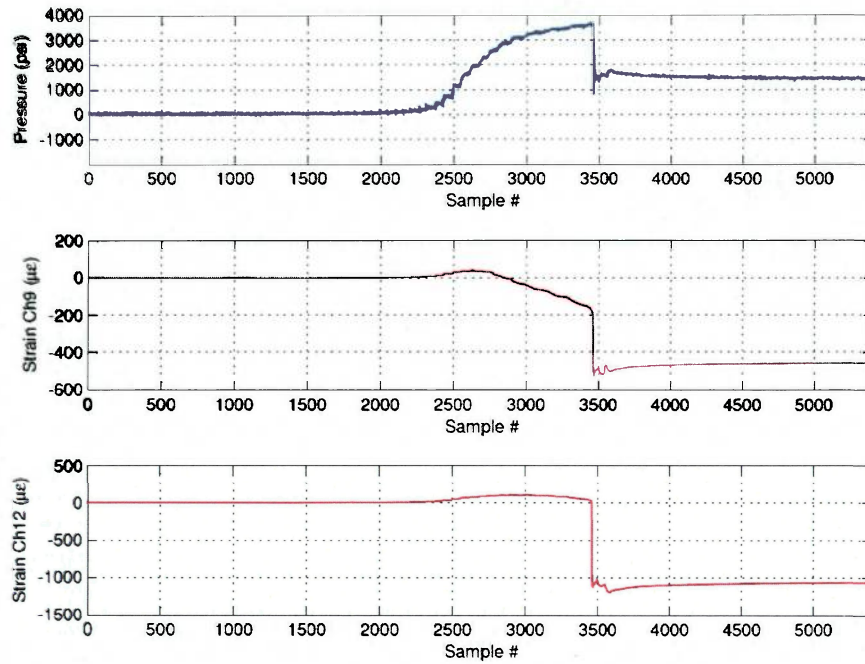


Figure 3-12. The graph for (Top) pressure, (Middle) channel 9 and (Bottom) channel 12.

### 3.2 Analysis

To determine if the SLS is Isotropic the HPT strain data is compared to the strain predicted by NASTRAN for an Isotropic material. The material properties used in the NASTRAN model are gathered from the material data sheet for EOS StrainlessSteel 17-4 on the EOS website and can be seen in Table 3-1 [7].

Table 3-1. The EOS StrainlessSteel 17-4 material properties.

Young's Modulus	Poisson's Ratio	Ultimate Tensile Strength	Yield Strength
28,000 ksi	0.27	130 ksi	73 ksi

The CATIA model of the tank is imported into NASTRAN to create the tanks geometry. The geometry is meshed using solid elements with 10 nodes per line.

An FEA analysis is run with internal pressure loads of 500, 1000, 1500, 2000, 2500 and 3000 psi.

To find NASTRAN data that can be compared to the HPT end-cap strain gage data, a rectangle with the dimensions of a strain gage is placed on the NASTRAN model at the average strain gage location for the end-cap gages. This process can be seen in Figure 3-13. The NASTRAN model strain data for the tetrahedrons within this rectangle are recorded for each analysis run. NASTRAN displays the strain values as effective strain, which is a function of the principle strains ( $\epsilon_1$ ,  $\epsilon_2$  and  $\epsilon_3$ ) and can be seen in Equation 3.

$$\epsilon_{effective} = \left(\frac{\sqrt{2}}{3}\right) [(\epsilon_1 - \epsilon_2)^2 + (\epsilon_2 - \epsilon_3)^2 + (\epsilon_3 - \epsilon_1)^2]^{\frac{1}{2}} \quad \text{Eq. 3}$$

The strain measured with the strain gages mounted to the tank is strain in the x, y or z direction depending on which gage is being measured. To get the NASTRAN strain data in the same form as the HPT strain so they can be compared Equations 4 [8] is used. Equation 5 [8] is the Strain-Displacement Matrix and is used in Equation 4. The components of the Strain-Displacement matrix ( $B_1$ ,  $B_2$ ,  $B_3$  and  $B_4$ ) can be found by using equation 6 [8] and replacing 'i' with the subscript of the component that is being calculated.

$$\{\epsilon\} = [B]\{d\} \quad \text{Eq. 4}$$

$$[B] = [B_1 B_2 B_3 B_4] \quad \text{Eq. 5}$$

$$B_i = \left(\frac{1}{6V}\right) \begin{bmatrix} \beta_i & 0 & 0 \\ 0 & \gamma_i & 0 \\ 0 & 0 & \delta_i \\ \gamma_i & \beta_i & 0 \\ 0 & \delta_i & \gamma_i \\ \delta_i & 0 & \beta_i \end{bmatrix} \quad \text{Eq. 6}$$

$$\beta_1 = - \begin{vmatrix} 1 & y_2 & z_2 \\ 1 & y_3 & z_3 \\ 1 & y_4 & z_4 \end{vmatrix} \quad \beta_2 = \begin{vmatrix} 1 & y_1 & z_1 \\ 1 & y_3 & z_3 \\ 1 & y_4 & z_4 \end{vmatrix} \quad \text{Eq. 7.a-b}$$

$$\beta_3 = - \begin{vmatrix} 1 & y_1 & z_1 \\ 1 & y_2 & z_2 \\ 1 & y_4 & z_4 \end{vmatrix} \quad \beta_4 = \begin{vmatrix} 1 & y_1 & z_1 \\ 1 & y_2 & z_2 \\ 1 & y_3 & z_3 \end{vmatrix} \quad \text{Eq. 8.a-b}$$

$$\delta_1 = - \begin{vmatrix} 1 & x_2 & y_2 \\ 1 & x_3 & y_3 \\ 1 & x_4 & y_4 \end{vmatrix} \quad \delta_2 = \begin{vmatrix} 1 & x_1 & y_1 \\ 1 & x_3 & y_3 \\ 1 & x_4 & y_4 \end{vmatrix} \quad \text{Eq. 9.a-b}$$

$$\delta_3 = - \begin{vmatrix} 1 & x_1 & y_1 \\ 1 & x_2 & y_2 \\ 1 & x_4 & y_4 \end{vmatrix} \quad \delta_4 = \begin{vmatrix} 1 & x_1 & y_1 \\ 1 & x_2 & y_2 \\ 1 & x_3 & y_3 \end{vmatrix} \quad \text{Eq. 10.a-b}$$

$$\gamma_1 = \begin{vmatrix} 1 & x_2 & z_2 \\ 1 & x_3 & z_3 \\ 1 & x_4 & z_4 \end{vmatrix} \quad \gamma_2 = - \begin{vmatrix} 1 & x_1 & z_1 \\ 1 & x_3 & z_3 \\ 1 & x_4 & z_4 \end{vmatrix} \quad \text{Eq. 11.a-b}$$

$$\gamma_3 = \begin{vmatrix} 1 & x_1 & z_1 \\ 1 & x_2 & z_2 \\ 1 & x_4 & z_4 \end{vmatrix} \quad \gamma_4 = - \begin{vmatrix} 1 & x_1 & z_1 \\ 1 & x_3 & z_3 \\ 1 & x_3 & z_3 \end{vmatrix} \quad \text{Eq. 12.a-b}$$

$$6V = \begin{vmatrix} 1 & x_1 & y_1 & z_1 \\ 1 & x_2 & y_2 & z_2 \\ 1 & x_3 & y_3 & z_3 \\ 1 & x_4 & y_4 & z_4 \end{vmatrix} \quad \text{Eq. 13}$$

$$\{d\} = \begin{Bmatrix} u_1 \\ v_1 \\ w_1 \\ \vdots \\ u_4 \\ v_4 \\ w_4 \end{Bmatrix} \quad \text{Eq. 14}$$

The original x, y and z coordinates and u, v and w translations of all four nodes for each tetrahedron can be obtained from NASTRAN. The data for each one of the pressure runs was determined and it is presented in Table 3-2.

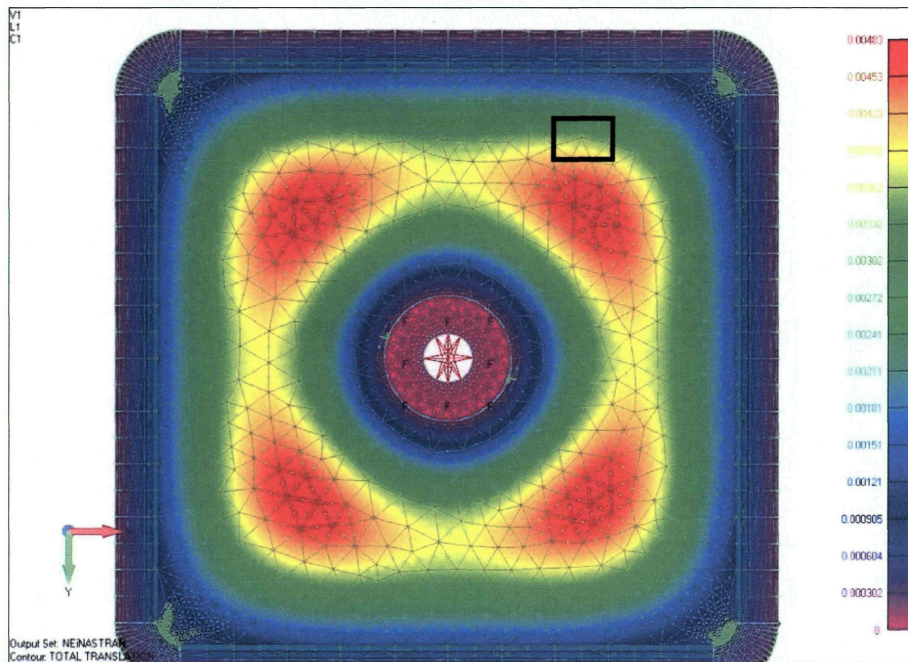


Figure 3-13. An example of the end-cap tetrahedron selection.

Table 3-2. The end-cap NASTRAN strain data.

Tetrahedron ID	500psi ( $\mu\epsilon$ )	1000psi ( $\mu\epsilon$ )	1500psi ( $\mu\epsilon$ )	2000psi ( $\mu\epsilon$ )	2500psi ( $\mu\epsilon$ )	3000psi ( $\mu\epsilon$ )
245133	230.8263337	461.6539402	692.4735552	923.3098624	1154.129477	1384.963803
267589	243.9849293	487.9728655	731.958372	975.9339918	1219.920597	1463.905759
419992	184.3254352	368.6505366	552.9791036	737.2981674	921.6344404	1105.956184
191712	188.8820014	377.7637438	566.6490903	755.525226	944.4169563	1133.294788
217438	149.0313354	298.0602337	447.0891618	755	745.1615811	894.1928867
155971	181.9836763	363.972999	545.9533984	727.9278742	909.9183816	1091.900873
282538	216.259583	432.5211704	648.7736664	865.0404081	1081.294837	1297.561578
Average	199.33	398.66	597.98	820.01	996.64	1195.97

The NASTRAN strain data is compared to equivalent HPT strain data, which is accomplished by choosing HPT strain data that is measured around the appropriate pressure value. The median values of the sample pressure data along with the distribution values of each sample group are shown in Figure 3-14. The edges of the boxes in the top graph in Figure 3-14 represent the 25<sup>th</sup> and 75<sup>th</sup> percentile while the whiskers represent the more extreme data points. Under each test sample group, in Figure 3-14, is a histogram of the pressure data distribution of the corresponding test sample group.

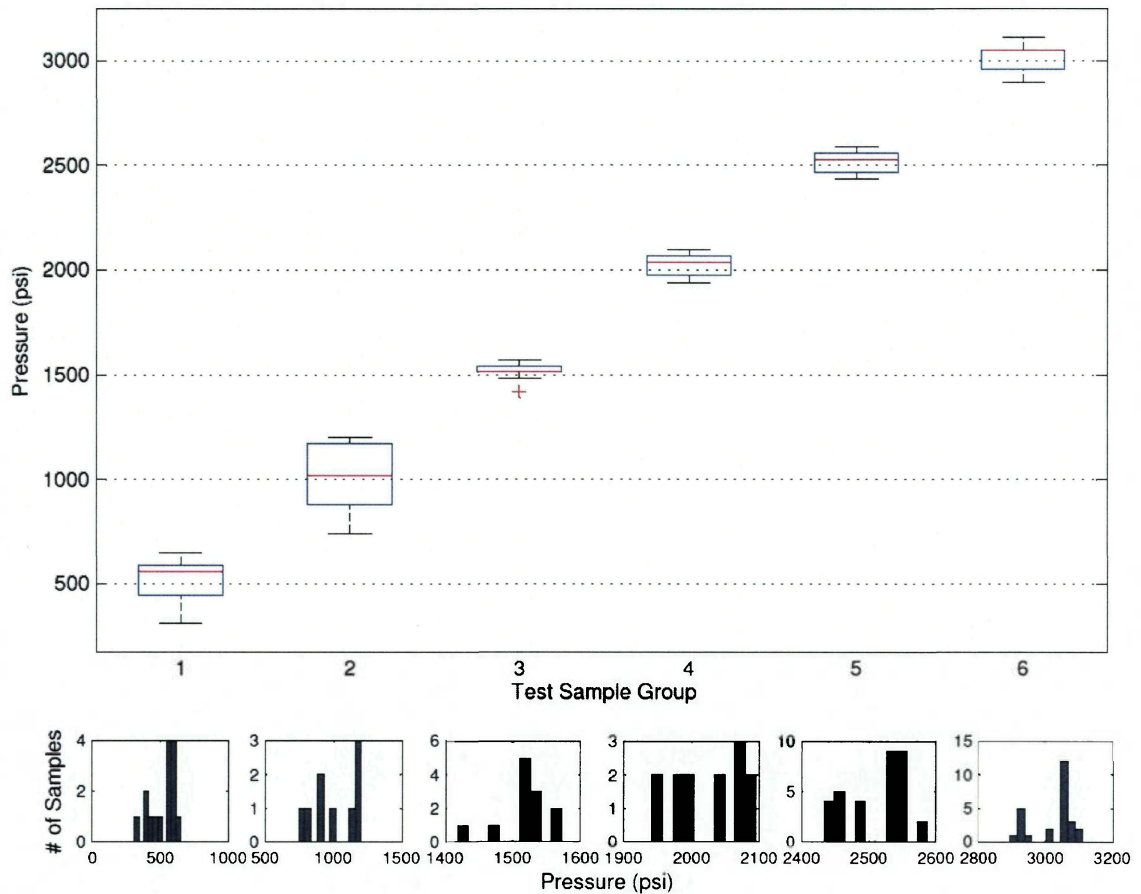


Figure 3-14. The end-cap sample median pressure value and distribution.

The HPT strain data around the appropriate pressure for end-cap strain channels 1,2 and 8 is gathered and averaged to give a good representation of the data for that pressure load at the end-caps. As noted before, channel 7 was excluded from the data because it deviates significantly from the other channels for the reasons stated in Section 3.1. This comparison data is shown in Table 3-3 along with the percent error between the NASTRAN data assuming isotropic materials and the average HPT data. The raw strain channel data for each relevant pressure are located in the appendix. The data is within 9% error up to 2000psi then starts to deviate significantly from the NASTRAN model. This is most likely due to plastic



deformation where the gage is measuring strain being compared to NASTRAN data that assumes elastic deformation. The stresses in several tetrahedrons at the 2500 and 3000psi NASTRAN test models are in fact above the yield strength of the material, which supports the theory that the larger percent error is due to entering the plastic deformation region.

Table 3-3. The end-cap strain data percent error.

Pressure (psi)	NASTRAN Strain Value ( $\mu\epsilon$ )	HPT Strain Value ( $\mu\epsilon$ )	% Error
500	199.33	198.33	-0.50
1000	398.66	404.07	1.36
1500	597.98	649.88	8.68
2000	820.01	892.31	8.82
2500	996.64	1148.42	15.23
3000	1195.97	1447.26	21.01

The process for gathering comparable data is repeated for the vertical side wall strain gages locations to compare to channels 4, 5, 10 and 11. The NASTRAN vertical side wall strain gage location data for the various pressure loads can be seen in Table 3-4. The 3000psi pressure data is not shown because the values gathered are the maximum values of the DAQ card meaning that the value being read is greater than or equal to the maximum value the card can read so the data is unreliable.

Table 3-4. The vertical side wall NASTRAN data.

Tetrahedron ID	500psi ( $\mu\epsilon$ )	1000psi ( $\mu\epsilon$ )	1500psi ( $\mu\epsilon$ )	2000psi ( $\mu\epsilon$ )	2500psi ( $\mu\epsilon$ )
214016	220.57824	441.156479	661.734719	882.312959	1102.8737
345991	630.17328	1260.34656	1890.51925	2520.69428	3150.86931
373357	630.17328	1260.34656	1890.51925	2520.69428	3150.86931
378761	137.24661	274.49905	411.745659	548.998101	686.244709
383077	256.74037	513.480747	770.221704	1026.96033	1283.70478
403220	832.07701	1664.14819	2496.2252	3328.30222	4160.3734
263106	108.03707	216.074143	324.102462	432.142451	540.176605
Average	402.15	804.29	1206.44	1608.59	2010.73

As before, the HPT strain data is compared to equivalent NASTRAN strain data. The median values of the sample pressure data along with the distribution values of each sample group are shown in Figure 3-15. Table 3-5 shows the comparison between the HPT data and the NASTRAN analysis data. The table shows that there is less than a 9% error for each of the pressure load analysis.

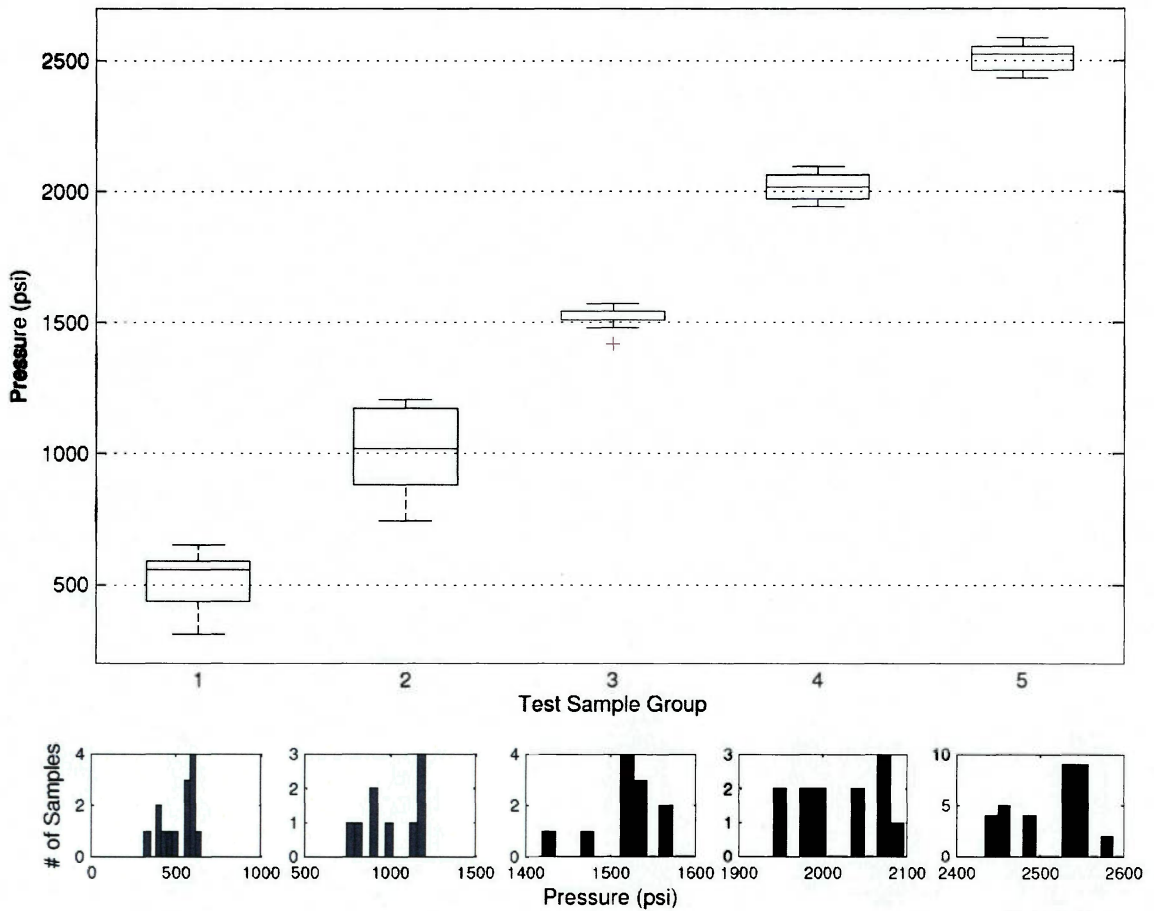


Figure 3-15. The vertical side wall sample median pressure and distribution.

Table 3-5. The vertical strain gage percent error.

Pressure (psi)	NASTRAN Strain Value ( $\mu\epsilon$ )	HPT Strain Value ( $\mu\epsilon$ )	% Error
500	402.15	394.14	-1.99
1000	804.29	788.56	-1.96
1500	1206.44	1261.68	4.58
2000	1608.59	1740.42	8.20
2500	2010.73	2170.09	7.93

## CONCLUSIONS

Strain data collected during a HPT of a stainless steel propellant tank, manufactured with SLS, has been compared to NASTRAN strain data which assumed isotropic material properties. It has been found that the strain data is within a 9% error before plastic deformation begins. The test results lead to the conclusion that the metal SLS propellant tank behaves close to one made of an isotropic material. The results of the tests also show that the tank has been overdesigned since the design pressure of 1300psi is exceeded by 2400psi at failure.

## RECOMMENDATIONS

The tank should be redesigned with walls of constant thickness instead of having the thicker end-caps than are currently used. The baffle should be extended all the way to the walls at the corners of the tank to potentially postpone initial baffle cracks. It would also be beneficial to perform fatigue testing due to thermal cycling.

Due to some of the strain gages being placed in less than optimal locations or insufficiently bonded to the tank and some data being unusable because of the limits of the DAQ cards being used, it is recommended that standard material properties test be conducted to positively confirm if metal SLS constructed parts are isotropic. These tests should include but not be limited to tension, compression, fatigue and impact tests.

## REFERENCES

- [1] EOS GmbH, *M270 Datasheet*
- [2] Ogando, Joseph. Rapid Manufacturing's Role in the Factory of the Future. *Design News*. [Online] August 12, 2007. [Cited: 1 25, 2011.]  
[http://www.designnews.com/article/7233-Rapid\\_Manufacturing\\_s\\_Role\\_in\\_the\\_Factory\\_of\\_the\\_Future.php](http://www.designnews.com/article/7233-Rapid_Manufacturing_s_Role_in_the_Factory_of_the_Future.php)
- [3] Vishay Precision Group. *Micro-Measurements*. [Online]  
<http://www.vishaypg.com/docs/11312/250uw.pdf>.
- [4] Vishay Precision Group. Strain Gage Installations with M-Bond 200 Adhesive. [Online]  
[http://www.me.ua.edu/me360/PDF/Strain\\_Gage\\_Installations\\_with\\_M-Bond\\_200\\_Adhesive.pdf](http://www.me.ua.edu/me360/PDF/Strain_Gage_Installations_with_M-Bond_200_Adhesive.pdf).
- [5] Omegadyne. [Online] <http://www.omega.com/Pressure/pdf/PX41-5V.pdf>.
- [6] National Instruments, *PCI-6221 and USB-6008 Datasheets*
- [7] EOS GmbH, *Material Property Datasheet for StrainlessSteel 17-4*
- [8] Daryl L. Logan. *A First Course in the Finite Element Method*. Toronto: Chris Carson, 2007.

## APPENDIX

The end-cap HPT data at 500psi.

Sample #	Strain Ch1 (μ€)	Strain Ch2 (μ€)	Strain Ch8 (μ€)	Pressure Ch13 (psi)
2423	188	143	183	404.24
2424	188	143	184	404.24
2425	187	143	183	496.49
2426	187	143	183	557.99
2427	187	143	183	311.99
2428	194	147	189	434.99
2429	206	157	202	588.74
2430	214	163	209	557.99
2431	222	170	217	465.74
2432	234	179	229	588.74
2433	245	187	239	588.74
2434	254	194	248	557.99
2435	263	201	256	650.24
2436	271	208	264	588.74
Channel Average	217.14	165.79	212.07	514.06
Total Strain Average	198.33			

The end-cap HPT data at 1000psi.

Sample #	Strain Ch1 (μ€)	Strain Ch2 (μ€)	Strain Ch8 (μ€)	Pressure Ch13 (psi)
2496	346	268	333	926.99
2497	355	275	342	742.49
2498	369	286	355	896.24
2499	386	299	371	1019.24
2500	393	304	377	834.74
2501	531	415	499	1142.24
2502	537	420	504	1203.74
2503	541	423	507	1172.99
2504	542	424	508	1172.99
Channel Average	444.44	346.00	421.78	1012.41
Total Strain Average	404.07			

The end-cap HPT data at 1500psi.

Sample #	Strain Ch1 ( $\mu\epsilon$ )	Strain Ch2 ( $\mu\epsilon$ )	Strain Ch8 ( $\mu\epsilon$ )	Pressure Ch13 (psi)
2565	684	537	631	1511.24
2566	692	544	638	1418.99
2567	699	550	644	1541.99
2568	709	557	652	1480.49
2569	715	562	657	1511.24
2570	723	568	664	1541.99
2571	729	574	669	1511.24
2572	735	579	674	1572.74
2573	742	584	680	1511.24
2574	747	588	684	1572.74
2575	753	593	689	1541.99
Channel Average	720.73	566.91	662.00	1519.63
Total Strain Average	649.88			

The end-cap HPT data at 2000psi.

Sample #	Strain Ch1 ( $\mu\epsilon$ )	Strain Ch2 ( $\mu\epsilon$ )	Strain Ch8 ( $\mu\epsilon$ )	Pressure Ch13 (psi)
2674	973	774	870	1941.74
2675	973	774	870	1972.49
2676	973	774	870	1941.74
2677	975	776	872	2003.24
2678	981	780	877	2034.00
2679	985	784	881	2003.24
2680	990	787	886	1972.49
2681	999	794	894	2064.75
2682	1006	800	901	2064.75
2683	1011	804	905	2034.00
2684	1017	809	911	2064.75
2685	1024	814	917	2095.50
2686	1029	819	921	2095.50
Channel Average	995.08	791.46	890.38	2022.17
Total Strain Average	892.31			



The end-cap HPT data at 2500psi.

Sample #	Strain Ch1 (μ€)	Strain Ch2 (μ€)	Strain Ch8 (μ€)	Pressure Ch13 (psi)
2745	1215	972	1076	2433.75
2746	1220	976	1080	2433.75
2747	1225	981	1084	2433.75
2748	1230	985	1089	2433.75
2749	1235	990	1093	2464.50
2750	1240	994	1097	2464.50
2751	1245	998	1101	2464.50
2752	1250	1002	1106	2526.00
2753	1255	1006	1109	2495.25
2754	1260	1010	1114	2464.50
2755	1265	1014	1117	2495.25
2756	1269	1018	1121	2464.50
2757	1274	1022	1125	2526.00
2758	1278	1025	1129	2556.75
2759	1283	1029	1133	2526.00
2760	1287	1033	1136	2526.00
2761	1291	1036	1139	2556.75
2762	1295	1039	1142	2495.25
2763	1298	1042	1145	2526.00
2764	1302	1045	1148	2526.00
2765	1304	1047	1150	2495.25
2766	1307	1050	1152	2526.00
2767	1310	1052	1154	2526.00
2768	1311	1054	1155	2526.00
2769	1314	1056	1158	2556.75
2770	1316	1058	1159	2556.75
2771	1318	1059	1161	2556.75
2772	1320	1061	1163	2587.50
2773	1322	1063	1163	2556.75
2774	1324	1064	1165	2556.75
2775	1325	1066	1166	2556.75
2776	1327	1067	1168	2556.75
2777	1329	1069	1169	2587.50
Channel Average	1283.15	1029.79	1132.33	2513.88
Total Strain Average	1148.42			

The end-cap HPT data at 3000 psi.

Sample #	Strain Ch1 (μ€)	Strain Ch2 (μ€)	Strain Ch8 (μ€)	Pressure Ch13 (psi)
2894	1543	1252	1348	2925.75
2895	1546	1255	1352	2895.00
2896	1549	1257	1354	2925.75
2897	1552	1259	1357	2956.50
2898	1556	1262	1360	2925.75
2899	1558	1265	1363	2925.75
2900	1561	1267	1365	2925.75
2901	1615	1312	1411	3018.00
2902	1618	1315	1414	3018.00
2903	1621	1318	1416	3048.75
2904	1624	1321	1419	3048.75
2905	1627	1323	1422	3048.75
2906	1630	1325	1424	3048.75
2907	1633	1328	1427	3079.50
2908	1636	1330	1428	3048.75
2909	1639	1333	1431	3079.50
2910	1641	1335	1433	3048.75
2911	1644	1337	1435	3048.75
2912	1646	1340	1437	3048.75
2913	1648	1341	1439	3048.75
2914	1651	1344	1441	3048.75
2915	1653	1346	1443	3110.25
2916	1654	1347	1444	3048.75
2917	1656	1349	1446	3048.75
2918	1658	1350	1447	3079.50
2919	1660	1352	1448	3110.25
Channel Average	1616.12	1313.96	1411.69	3021.55
Total Strain Average	1447.26			

The vertical sidewall HPT data at 500psi.

Sample #	Strain Ch5 ( $\mu\epsilon$ )	Strain Ch11 ( $\mu\epsilon$ )	Pressure Ch13 (psi)
2423	243	425	404.24
2424	243	422	404.24
2425	243	424	496.49
2426	243	424	557.99
2427	243	438	311.99
2428	252	469	434.99
2429	268	484	588.74
2430	279	504	557.99
2431	289	532	465.74
2432	305	555	588.74
2433	320	575	588.74
2434	330	593	557.99
2435	342	612	650.24
2436	352	627	588.74
Channel Average	282.29	506.00	514.06

The vertical sidewall HPT data at 1000psi.

Sample #	Strain Ch5 ( $\mu\epsilon$ )	Strain Ch11 ( $\mu\epsilon$ )	Pressure Ch13 (psi)
2496	451	792	926.99
2497	462	823	742.49
2498	481	860	896.24
2499	503	871	1019.24
2500	512	898	834.74
2501	700	1169	1142.24
2502	709	1177	1203.74
2503	713	1177	1172.99
2504	715	1181	1172.99
Channel Average	582.89	994.22	1012.41

The vertical sidewall HPT data at 1500psi.

Sample #	Strain Ch5 ( $\mu\epsilon$ )	Strain Ch11 ( $\mu\epsilon$ )	Pressure Ch13 (psi)
2565	918	1481	1511.24
2566	929	1495	1418.99
2567	941	1515	1541.99
2568	954	1527	1480.49
2569	964	1542	1511.24
2570	975	1555	1541.99
2571	985	1567	1511.24
2572	994	1581	1572.74
2573	1003	1589	1511.24
2574	1012	1602	1572.74
2575	1020	1608	1541.99
Channel Average	972.27	1551.09	1519.63

The vertical sidewall HPT data at 2000psi.

Sample #	Strain Ch5 ( $\mu\epsilon$ )	Strain Ch11 ( $\mu\epsilon$ )	Pressure Ch13 (psi)
2674	1368	2029	1941.74
2675	1369	2027	1972.49
2676	1369	2034	1941.74
2677	1372	2048	2003.24
2678	1381	2055	2034.00
2679	1388	2070	2003.24
2680	1395	2087	1972.49
2681	1408	2104	2064.75
2682	1420	2113	2064.75
2683	1427	2125	2034.00
2684	1438	2143	2064.75
2685	1449	2151	2095.50
Channel Average	1398.67	2082.17	2016.06

The vertical sidewall HPT Data at 2500 psi.

Sample #	Strain Ch5 ( $\mu\epsilon$ )	Strain Ch11 ( $\mu\epsilon$ )	Pressure Ch13 (psi)
2745	1788	2417	2433.75
2746	1797	2417	2433.75
2747	1807	2417	2433.75
2748	1817	2417	2433.75
2749	1827	2417	2464.50
2750	1837	2417	2464.50
2751	1846	2417	2464.50
2752	1856	2417	2526.00
2753	1866	2417	2495.25
2754	1875	2417	2464.50
2755	1885	2417	2495.25
2756	1894	2417	2464.50
2757	1904	2417	2526.00
2758	1912	2417	2556.75
2759	1921	2417	2526.00
2760	1929	2417	2526.00
2761	1937	2417	2556.75
2762	1946	2417	2495.25
2763	1952	2417	2526.00
2764	1959	2417	2526.00
2765	1965	2417	2495.25
2766	1971	2417	2526.00
2767	1976	2417	2526.00
2768	1981	2417	2526.00
2769	1986	2417	2556.75
2770	1990	2417	2556.75
2771	1994	2417	2556.75
2772	1999	2417	2587.50
2773	2002	2417	2556.75
2774	2006	2417	2556.75
2775	2010	2417	2556.75
2776	2013	2417	2556.75
2777	2017	2417	2587.50
Channel Average	1923.18	2417.00	2513.88